

# JGR Solid Earth

## RESEARCH ARTICLE

10.1029/2022JB026232

### Key Points:

- Constraints from topography and strain model enable the retrieval of complete 3-D movements for landslides using multi-source SAR datasets
- The potential of novel features of forthcoming NISAR datasets in deriving accurate 3-D movements for landslides is demonstrated
- 3-D deformation field yields key insights into the Xinpu landslide's movement patterns, basal geometry, and hydrological influence

### Supporting Information:

Supporting Information may be found in the online version of this article.

### Correspondence to:

J. Hu,  
csuhujun@csu.edu.cn

### Citation:

Zheng, W., Hu, J., Lu, Z., Hu, X., Sun, Q., Liu, J., et al. (2023). Enhanced kinematic inversion of 3-D displacements, geometry, and hydraulic properties of a north-south slow-moving landslide in Three Gorges Reservoir. *Journal of Geophysical Research: Solid Earth*, 128, e2022JB026232. <https://doi.org/10.1029/2022JB026232>

Received 12 DEC 2022  
Accepted 5 JUN 2023

### Author Contributions:

**Conceptualization:** Wanji Zheng, Jun Hu, Jihong Liu  
**Data curation:** Jianjun Zhu  
**Formal analysis:** Wanji Zheng, Zhong Lu  
**Funding acquisition:** Jun Hu  
**Investigation:** Wanji Zheng  
**Methodology:** Wanji Zheng, Jun Hu, Xie Hu, Jihong Liu  
**Project Administration:** Jun Hu  
**Resources:** Zhiwei Li  
**Software:** Jianjun Zhu, Zhiwei Li  
**Supervision:** Jun Hu  
**Validation:** Wanji Zheng, Qian Sun  
**Visualization:** Wanji Zheng  
**Writing – original draft:** Wanji Zheng

© 2023. American Geophysical Union.  
All Rights Reserved.

## Enhanced Kinematic Inversion of 3-D Displacements, Geometry, and Hydraulic Properties of a North-South Slow-Moving Landslide in Three Gorges Reservoir

Wanji Zheng<sup>1,2</sup> , Jun Hu<sup>1,3</sup> , Zhong Lu<sup>2</sup> , Xie Hu<sup>4</sup> , Qian Sun<sup>5</sup> , Jihong Liu<sup>1</sup> , Jianjun Zhu<sup>1</sup>, and Zhiwei Li<sup>1</sup> 

<sup>1</sup>School of Geosciences and Info-Physics, Central South University, Changsha, China, <sup>2</sup>Roy M. Huffington Department of Earth Sciences, Southern Methodist University, Dallas, TX, USA, <sup>3</sup>Hunan Geological Disaster Monitoring, Early Warning and Emergency Rescue Engineering Technology Research Center, Changsha, China, <sup>4</sup>College of Urban and Environmental Sciences, Peking University, Beijing, China, <sup>5</sup>College of Resources and Environmental Science, Hunan Normal University, Changsha, China

**Abstract** Complete three-dimensional (3-D) movements of slow-moving landslides are critical to enhancing the understanding of the landslide mechanism. Multi-source synthetic aperture radar (SAR) observations provide an opportunity to derive 3-D movements. However, deriving the complete 3-D movements faces potential challenges of incoherent phases and an ill-posed inverse problem, which may result in incomplete and inaccurate results, especially for slopes facing north/south. Here, we propose a topography-constrained strain model, which exploits the spatial relationship of 3-D deformations between neighboring points as well as the assumption of the surface parallel flow of landslide, to derive complete 3-D movements. Both synthetic and real datasets over the north-south Xinpu landslide complex are utilized, to assess if the implemented method can overcome the ill-posed condition and retrieve the complete 3-D movement field. With the multi-source SAR datasets, the performance of various datasets and the potential of NISAR in deriving time series and 3-D movements are assessed. Based on the derived complete 3-D movements and long-term InSAR measurements, the landslide metrics, including elementary parameters of landslide geometry, spatial-temporal patterns of movement, thickness, and hydraulic diffusivity, are derived to reveal that (a) the thickest landslide mass concentrates in the toe of the landslide, and (b) the effects of precipitation are more significant than those of the water level fluctuation in the Xinpu landslide complex, Three Gorges Reservoir areas.

**Plain Language Summary** Landslides are a dangerous geological phenomenon that can be difficult to monitor in site. Researchers have used radar remote sensing technology (i.e., SAR) to study landslides, which can provide valuable information about how they move and change over time. However, there are challenges in accurately estimating the complete three-dimensional (3-D) deformations, especially when landslides are facing north or south. In this study, we developed a new method to derive complete and accurate 3-D deformations for landslides by using multi-source SAR observations. The method was firstly tested on the simulated data, and then successfully applied in the Xinpu landslide complex in Three Gorges Reservoir area, China. Based on the derived 3-D deformations, the characteristics of the landslide, including movement patterns, basal geometry, and hydrological influence, were investigated. Our findings suggest that rainfall has greater impacts on landslide than changes in water levels, and a significant transport tunnel is located from the middle to the submerged region. These novel insights can help researchers better understand the causes and effects of landslides and potentially improve efforts to mitigate their impacts.

## 1. Introduction

As a type of frequent geohazard, landslides affect many regions worldwide and cause catastrophic consequences (Lacroix et al., 2020; Petley, 2012). Rainfall, hydrological processes, earthquakes, and human activities usually increase the ratio of failure shear stress to resisting shear strength, resulting in a decrease in slope stability. During past decades, interferometric synthetic aperture radar (SAR, InSAR) has been playing a significant role in monitoring landslide deformation due to its all-weather, high-precision, and wide-coverage features. In particular, the derivation of three-dimensional (3-D) movement can overcome the limitations of line-of-sight (LOS) observation and provide new insights for understanding landslides, such as the exploration of the new kinematic unit

**Writing – review & editing:** Wanji Zheng, Jun Hu, Zhong Lu, Xie Hu, Qian Sun

(Delbridge et al., 2016), the derivation of landslide thickness (X. Hu et al., 2019), and the estimation of strain rate (Handwerger et al., 2019).

By integrating more than three independent InSAR measurements with significant differences in observation geometries and solving using the weighted least-square (WLS) method, the 3-D deformation field can be derived (J. Hu, Li, et al., 2014). However, space-borne InSAR datasets with significant viewing angle differences can only be achieved in high-latitude areas (Zheng et al., 2017). In addition, the InSAR measurement is insensitive to the north-south movement. Even if more than three independent InSAR measurements are available, for the north-south slope, the ill-posed problem could reduce the reliability of the derived 3-D movements (J. Hu, Li, et al., 2014). Deriving 3-D deformations constrained by some models is the optimal solution for specific geophysical events, which can significantly reduce the requirement of datasets and has been implemented in many fields, associated with volcanoes (J. Hu et al., 2017), glaciers (Samsonov, 2019), and subsidence (Murray et al., 2021; Yang et al., 2017). The surface-parallel flow (SPF) constraint, as the primary geo-prior-based method for deriving landslide movements, estimates the 3-D movements of slow-moving landslides by establishing the relationship between vertical and horizontal deformations based on the gradient of aspect and slope (Joughin et al., 1998; Samsonov, 2019). The method is able to obtain 3-D movements with only two datasets in distinct geometries, which has been proven effective in various cases. However, while the slope aspect is north-south, the corresponding coefficient matrix will lead to an ill-conditioned model, which means that the SPF method will fail to derive reliable 3-D deformation. This problem can be eased by introducing the azimuth (AZI) deformation generated by pixel offset tracking (POT) technique (Michel et al., 1999) or multi-aperture InSAR (MAI) (Bechor & Zebker, 2006). However, such methods are generally available for geophysical events with large deformation (e.g., earthquakes, volcanic eruptions, and glacier movements). For slow-moving landslides, MAI/POT-derived measurements usually fail to derive an accurate spatially complete deformation field because of the spatial resolution and signal-to-noise ratio (SNR) of SAR data.

With the increasing need for SAR-related products, more and more space-borne SAR platforms have been operated in orbit with distinct frequencies, spatial resolutions, and features, which provide additional sights and datasets for estimating 3-D movements. In this study, we implement specific methods to derive the optimal deformation observations from multi-source SAR datasets (i.e., L-band ALOS2 PALSAR2, C-band Sentinel-1A, and X-band TanDEM-X) on the basis of corresponding characteristics. An SPF-constrained strain model (referred to as SPFS) is then proposed, integrating the measurements from multi-source SAR datasets to estimate the complete 3-D movements of slow-moving landslides. The strain model (SM) is a displacement-strain incremental equation model representing the connection between the 3-D displacement of proximal points (J. Li et al., 2019). Introducing the SM, the fragmentary deformation field can be effectively reconstructed with these strain constraints of adjacent points. However, when the SM is used to derive 3-D landslide movements, it may encounter an ill-posed problem. The SPFS addresses this issue by incorporating SPF constraints into the SM, thereby enhancing the reliability of 3-D deformation estimation. Additionally, because of the virtual observations, the variance components estimator (VCE) has also been improved for the final solution.

In order to assess the performance of the proposed method, both the synthetic and the real dataset experiments over the Xinpu landslide complex, referred to as the Three Gorges Reservoir (TGR) areas, are implemented. Known as the largest hydraulic project, the TGR began construction in 1994. Since the impoundment of the reservoir in 2008, the complicated geologic environment and the widespread unstable slopes have usually led to landslide disasters in conjunction with hydraulic processes (B. Huang et al., 2012; C. Li et al., 2019; Shi et al., 2015). However, because of the north-south aspect of most slopes and the dense vegetation, it is challenging to derive 3-D landslide movements in TGR areas. Only some efforts have been made to derive the 3-D movements from POT/MAI measurements with the assistance of sparse corner reflectors (Shi et al., 2015, 2017a). The Xinpu landslide complex is one of the giant landslides in the TGR area, and instability threatens residents. In recent years, significant movements have damaged roads and buildings (Figure S1 in Supporting Information S1). Here, we derive the complete 3-D deformation field of the Xinpu landslide complex by using L-band ALOS2 data, C-band Sentinel-1 data, and X-band TanDEM-X data from 2019 to 2022. The geometry and hydraulic properties are further explored on the basis of pixel-by-pixel 3-D movements in an attempt to better understand the mechanisms of the Xinpu landslide complex.

## 2. Study Area and Materials

The TGR project, currently the largest hydraulic project, is located on the Yangtze River. Similar to most reservoirs, the water level fluctuation has led to more than 2,400 landslides in the TGR areas (C. Li et al., 2019), particularly the Qianjiangping landslide, which resulted in 24 fatalities and approximately 1k injuries during the initial impoundment period in 2003 (S. Li et al., 2018). There are still many slow-moving landslides during the stable operation stage. In (Shi et al., 2016), approximately 30 slow-moving landslides were identified in the TGR area spanning from Fengjie county to Zigui county with multi-path ALOS PALSAR datasets. Several studies have been conducted to research the mechanism of landslides in the TGR area, which suggests that water level fluctuation is the key trigger that affects the stability of the reservoir bank slope (C. Li et al., 2019; Shi et al., 2015; Tomás et al., 2014).

Here we investigate the Xinpu landslide complex, which is located in southwest Fengjie County, which is close to the southern shore of the Yangtze River (Figure 1a). As one of the giant landslides in the TGR area, the deep-seated ( $>10$  m) bedded landslide has a length of 2,493 m, an average width of 1,160 m, and a volume of  $4.0 \times 10^7$  m<sup>3</sup>. The movement is affected by the sliding bed and lithology, the Xinpu landslide complex is formed by three independent slumping bodies, that is, XiaErTai (XET) slope, ShangErTai (SET) slope, and DaPing (DP) slope (Figure 1b). Previous study and in-situ investigation show that the Upper Triassic Xujiahe Formation (T<sub>3</sub>xj) and Lower Jurassic Zhenzhuchong Formation (J<sub>1z</sub>) comprises the bedrock, and the main components of the sliding masses are the Quaternary Holocene deposits (Q<sub>4</sub><sup>col+dl</sup> and Q<sub>4</sub><sup>del</sup>), which are made up of the gravel mixed with silty clay (Ye et al., 2023).

The water level of the Yangtze River rose from 135 to 175 m in 2008. Most of the toes of the landslides have been submerged by the river in the TGR area (Shi et al., 2015; Tomás et al., 2014). Similarly, the toe of the Xinpu landslide complex is also submerged under the water (Figure 1c), so the hydraulic process may affect the stability of the Xinpu landslide complex. The in-situ investigations between 2003 and 2006 showed that the XET and SET slopes experienced obvious surface deformations. In recent years, the XET slope, as the most extensive section of the Xinpu landslide complex with a total volume of  $3.4 \times 10^7$  m<sup>3</sup>, experienced noticeable ground movements, which caused many cracks in local houses and roads (Figure S1 in Supporting Information S1). Several GNSS stations have been installed in the XET slope to monitor movements since the end of 2019 (Figures 1b and 1c) (Q. Zhang et al., 2022a). To obtain real-time measurements for geohazard warnings, 3-D time series deformation is derived using the GNSS-RTK technique (G. Huang et al., 2021), with G1 serving as the reference station and G2 through G6 as monitoring stations. Since the complicated mobility of the Xinpu landslide complex is related to fluctuations in the hydraulic process in a large region, it is not enough to study the Xinpu landslide complex with such a few GNSS measurements.

To obtain the kinematics of the Xinpu landslide complex, we utilized the L-band ALOS2 PALSAR2, C-band Sentinel-1, and X-band TanDEM-X data from the end of 2019 to early 2022 to derive the 3-D movement field (Figure 1a). We note that the High-Resolution Spotlight TanDEM-X dataset was utilized to improve the POT measurements' performance (Table 1). The GNSS measurements shown in Figure 1b were then used to validate the results derived by the integration of multi-source SAR observations. Furthermore, we collected the daily precipitation records during 2005–2022 from NOAA (station #57348), which is located 17 km away from the landslide (Figure 1a). The precipitation records will be utilized to derive the diffusivity and pore-water pressure.

## 3. Methodology

This study collected the multi-source SAR datasets in the Xinpu landslide complex. SAR datasets at different frequencies exhibit variations in their wavelengths, beam modes, and pixel spacing. Optimization of the 1-D deformation measurements from multi-geometry, multi-frequency SAR data facilitates the estimation of accurate 3-D deformations. This section describes the methods for deriving the optimized deformation from each SAR dataset. Subsequently, the SPFS method is introduced to obtain the complete 3-D deformations on the basis of the SPF method and SM.

### 3.1. Derivation of the Deformations Based on the Features of the Multi-Source SAR Data

ALOS2 PALSAR2 is an L-band sensor launched into orbit in 2014. Although this satellite provides a 14-day repeat cycle, it is difficult to obtain regular observations in most areas (e.g., only six scenes of data can be

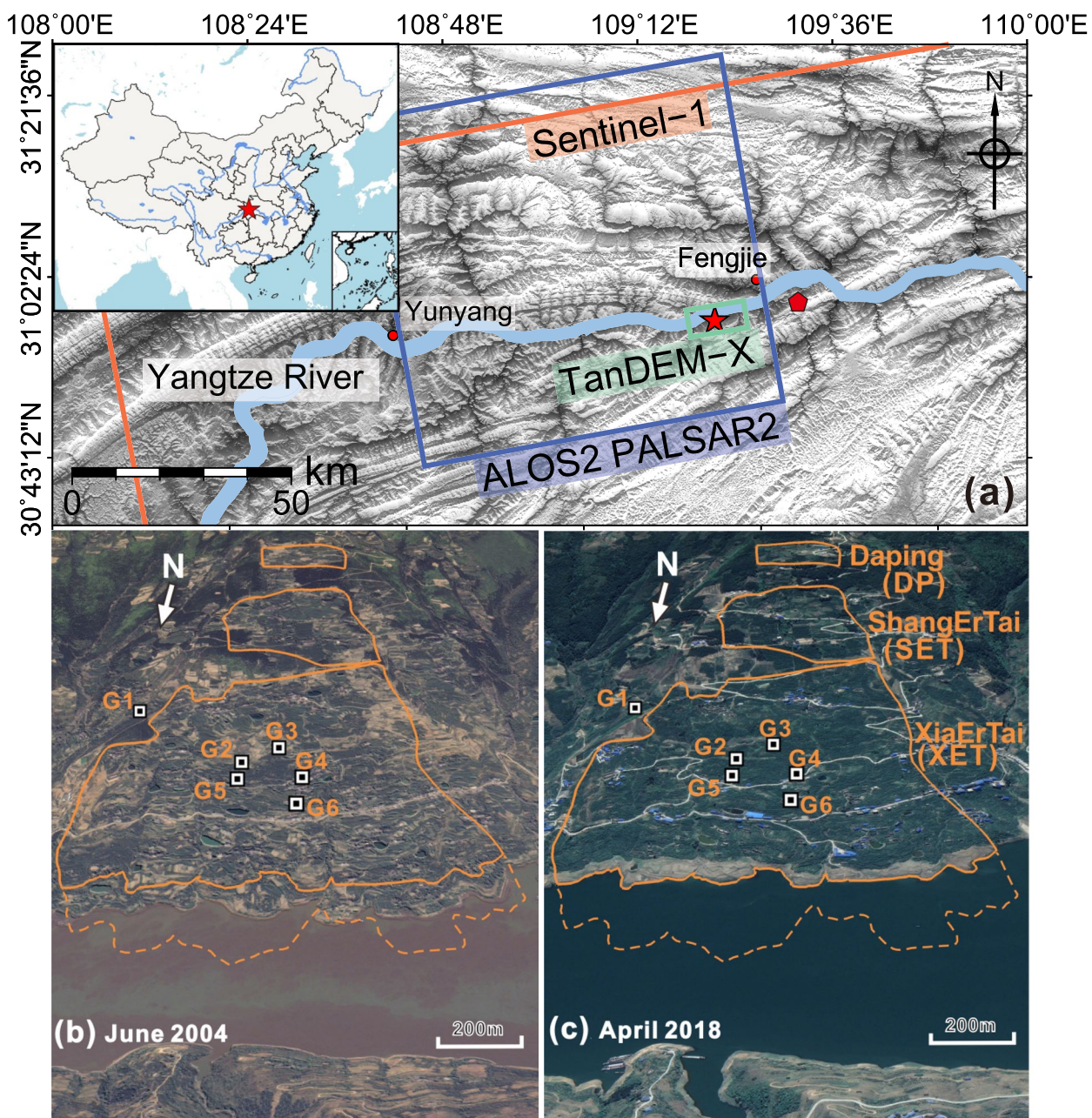


**Figure 1.** Location of the Xinpu landslide complex. (a) The footprint of the L-band ALOS2 PALSAR2 (orange box), C-band Sentinel-1A (blue box), and X-band TanDEM-X datasets (green box), superimposed on the shaded relief map. The Xinpu landslide complex (red star) lies between the Fengjie and Yunyang counties (red dots). The red pentagon is the location of the weather station. The inset is a sketch map of China. (b), (c) Google Earth image of the Xinpu landslide complex before and after the impoundment from 135 to 175 m. The Xinpu landslide complex is composed of the XiaErTai (XET) slope (including the submerged area shown as the orange dashed line), ShangErTai (SET) slope, and DaPing (DP) slope. G1 - G6 (squares) are the locations of GNSS stations, and G1 is a reference station located in a stable area outside the Xinpu landslide complex. The solid orange lines indicate the landslide boundary.

obtained in the Xinpu landslide complex during 2019–2022). However, the long wavelength and short perpendicular baseline are unique advantages of this SAR dataset for overcoming the decorrelation and for obtaining reliable phase in the area with dense vegetation. To optimize the result with more interferograms, the large temporal baseline of 700 days and the small perpendicular baseline of 250 m are set to generate 30 interferograms (Figure 2). The 30 m Copernicus DEM is then employed to eliminate the topographic components, and the minimum cost flow is utilized to unwrap the phase. Subsequently, a standard workflow of small baseline subsets (SBAS) (Berardino et al., 2002) is implemented to derive the LOS deformation.

**Table 1**  
*Basic Information of the Utilized SAR Datasets*

Sensor	ALOS2 PALSAR2	Sentinel-1A	TanDEM-X
Flight direction	Ascending	Ascending	Ascending
Span (yyyymmdd)	20200201–20220101	20191126–20220102	20191124–20220102
Number of scenes	6	60	12
Wavelength (cm)	24.3 (L-band)	5.6 (C-band)	3.1 (X-band)
Beam mode	Strimap	Interferometric Wide Swath	High-Resolution Spotlight
Incidence angle (°)	37.98	38.41	45.73
Heading (°)	−10.26	−10.36	−9.44
Pixel spacing (m) in Rg × Az	2.15 × 3.78	2.33 × 13.95	0.91 × 0.86

The C-band Sentinel-1 started a new era for InSAR with a regular revisit period of 6–12 days. Although the short revisit period is beneficial for obtaining high-coherence observations, the 5.6 cm-long wavelength usually leads to decorrelation over vegetated regions. To overcome the effect of decorrelation, the small temporal baseline of 36 days and a spatial baseline of 150 m are set to generate 112 interferograms from 60 scenes of SAR observations (Figure 2). Then, an ICA-assisted intermittent MTI method is implemented to derive the optimized deformation field. This method utilizes the intermittently coherent points to determine the spatially complete observations, and a Delaunay triangulation network is then built to connect the intermittent points. After a spatially integrating operation, the deformation can be estimated from each arc in the Delaunay network. Since the low threshold for selecting the intermittent points could decrease the reliability of deformation, the method exploits the ICA algorithm to derive reliable deformation signals based on the high spatial resolution of InSAR observations (see the Supporting Information).

TanDEM-X has the shortest wavelength among current space-borne SAR missions. The X-band signal is susceptible to decorrelation, and it is problematic to obtain a reliable interferometric phase in landslides with vegetation. However, the high-resolution spotlight mode of TanDEM-X can provide SAR data with the pixel spacing of the submeter (Table 1), which is beneficial to obtain reliable POT measurements. The azimuth deformation estimated from the POT measurements is critical for solving the ill-posed problem and deriving the 3-D deformations. However, since the POT measurements are insensitive to the small movements, we set a temporal baseline of at least 90 days for the POT pairs to include appreciable landslide movement, and the pixel-offset SBAS method (Casu et al., 2011) is subsequently utilized to improve the performance of the azimuth deformation (Figure 2). Nevertheless, the vegetation and large-gradient deformation would decrease the SNR of the measurement, resulting in an incomplete deformation field.

### 3.2. Optimization of the 3-D Deformations by the Surface Parallel Flow-Constrained Strain Model

#### 3.2.1. Background of 3-D Deformation Inversion and Surface-Parallel Flow Assumption

The LOS/azimuth deformation measured by SAR observation is the linear integration of the east, north, and up movement components. Therefore, solving a linear equation  $D^i = B^i \cdot X^i$  composed of three independent observations allow us to derive the 3-D movements (J. Hu, Li, et al., 2014). Here,  $D^i = [v_1^i \ v_2^i \ v_3^i]$  is the derived deformation associated with point  $p^i$  from Sentinel-1A, ALOS2 PALSAR2, and TanDEM-X datasets, respectively.  $X^i = [v_e^i \ v_n^i \ v_u^i]^T$  are the east, north, and up components of the 3-D deformation, respectively, and  $B^i = [(B_1^i)^T \ (B_2^i)^T \ (B_3^i)^T]^T$  is the transform matrix. The unit vectors  $B_1^i = [a_1^i \ b_1^i \ c_1^i]$ ,  $B_2^i = [a_2^i \ b_2^i \ c_2^i]$ , and  $B_3^i = [d_3^i \ e_3^i \ 0]$  are composed of the corresponding radar incidence angles  $\theta_j^i$  ( $j = 1, 2, 3$ ) and the satellite heading  $\alpha_j^i$  (clockwise from the north) for the  $j$  th SAR-related observations associated with point  $p^i$ .

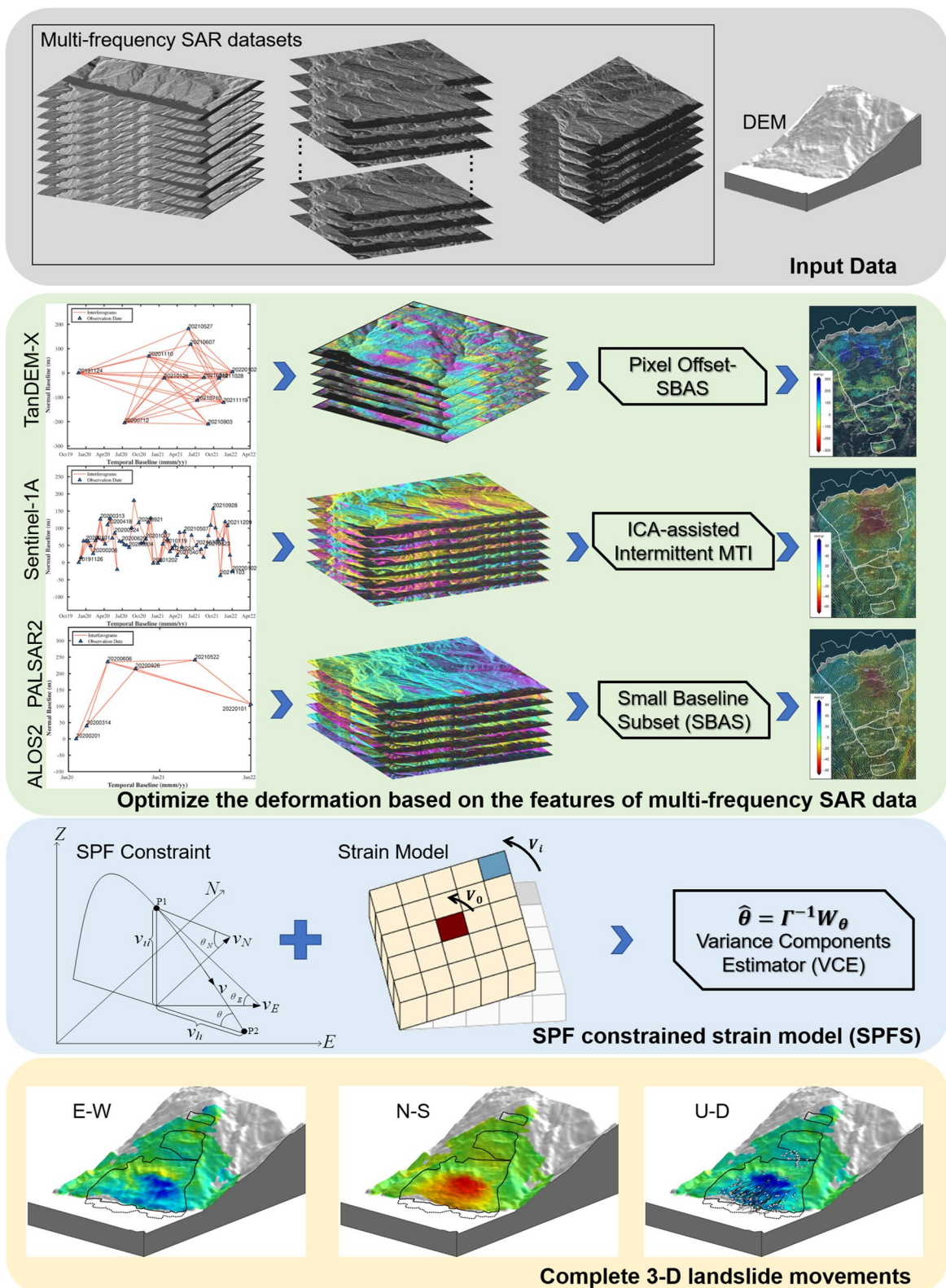


**Figure 2.** Schematic view of the utilized methods used in this study. See Section 3 and the Supporting Information for details on each step.

$$\text{where } \begin{cases} a_j^i = -\sin(\theta_j^i) \cdot \sin(\alpha_j^i - 3\pi/2) \\ b_j^i = -\sin(\theta_j^i) \cdot \cos(\alpha_j^i - 3\pi/2) \\ c_j^i = \cos(\theta_j^i) \\ d_j^i = -\cos(\alpha_j^i - 3\pi/2) \\ e_j^i = -\sin(\alpha_j^i - 3\pi/2) \end{cases} .$$

Although the 3-D movements  $X^i$  can be in theory estimated by weighted least square (WLS) adjustment, similar imaging geometries of different datasets usually leads to an ill-posed problem (Zheng et al., 2017). The SPF assumption is a common method for deriving the 3-D deformations in deep-seated slow-moving landslides (X. Hu et al., 2018; Ren et al., 2022). The assumption under consideration utilizes topographical information to constrain surface deformation. Specifically, it assumes that the ratio of 3-D deformation is proportional to the slope gradient and aspect of the terrain (i.e.,  $v_u/v_h = \text{slope}$ ;  $v_e/v_n = \text{aspect}$ ) (Joughin et al., 1998). The slope can be expressed as the magnitude of the gradient in the east and north directions (i.e.,  $\text{slope} = \sqrt{\theta_e^2 + \theta_n^2}$ ). Therefore, the 3-D deformation can be constrained by the slope gradient and aspect, where  $v_u$  can be expressed as a linear combination of the east and north slope components (i.e.,  $v_u = \theta_e \cdot v_e + \theta_n \cdot v_n$ ) and  $v_e$  can be expressed as a scalar multiple of  $v_n$  (i.e.,  $v_e = \text{aspect} \cdot v_n$ ). By incorporating this assumption, some virtual observations can be introduced into the observations, and the ill-posed problem of surface deformation estimation can be resolved. In this study, this method is utilized to ease the ill-posed condition. Note that this method is inappropriate for deriving the deformation primarily in the north/south direction because of the large condition number caused by the aspect constraint. Therefore, we only implement the slope constraint  $v_u^i = \theta_e^i \cdot v_e^i + \theta_n^i \cdot v_n^i$  to derive the 3-D movements, and the relationship between observations and 3-D movements can then be represented by

$$D_{SPF}^i = B_{SPF}^i \cdot X^i, \quad (1)$$

where  $D_{SPF}^i = [D^i \ 0]^T$  is the observation vector and  $B_{SPF}^i = [(B_1^i)^T \ (B_2^i)^T \ (B_3^i)^T \ (B_4^i)^T]^T$  is a transformation matrix. The constrained matrix  $B_4^i$  can be derived from the east components  $\theta_e^i$  and north components  $\theta_n^i$  of the slope gradient (J. Hu, Li, et al., 2014)

$$B_4^i = [-\theta_e^i \ -\theta_n^i \ 1],$$

Then, the 3-D movements can be derived by solving the unknowns of Equation 1. However, the vegetation and large-scale deformation usually decrease the SNR of POT measurements and lead to incomplete deformation.

### 3.2.2. Surface Parallel Flow-Constrained Strain Model

The displacement of the neighboring points on the landslide can be linked by some geophysical relationships. An example of this is the elastically coupled solution in which the connection between horizontal subsurface forces and displacement is built to improve the performance of deriving groundwater-induced 3-D deformations (Murray et al., 2021). The strain tensor is another connection that describes the strain constraints of the 3-D deformations among the neighboring points and had been implemented in the study of landslides (Handwerger et al., 2019). Here, the strain-tensor-related SM is introduced to the SPF constraint to rebuild the complete 3-D deformation field. Assume  $v^0 = [v_e^0 \ v_n^0 \ v_u^0]^T$  are the 3-D deformations at a point of interest  $P^0$  with position  $p^0 = [p_e^0 \ p_n^0 \ p_u^0]^T$ , and  $v^i = [v_e^i \ v_n^i \ v_u^i]^T$  is the 3-D deformation in a neighboring point  $P^i$ , ( $i = 1, 2, 3, \dots, n$ ) with position  $p^i = [p_e^i \ p_n^i \ p_u^i]^T$ . The displacement-strain relationship can be expressed as (J. Li et al., 2019)

$$v^i = H \cdot \Delta p^i + v^0, \quad (2)$$

where  $\Delta p^i = p^i - p^0$  is the position difference vector from point  $P^0$  to point  $P^i$ , and  $H = S + A$  is the movement gradient matrix. The symmetric matrix  $S$  and anti-symmetric matrix  $A$  can be represented by the strain tensor  $\zeta$  and rotation tensor  $\omega$

$$H = S + A = \begin{bmatrix} \zeta_{ee} & \zeta_{en} & \zeta_{eu} \\ \zeta_{en} & \zeta_{nn} & \zeta_{nu} \\ \zeta_{eu} & \zeta_{nu} & \zeta_{uu} \end{bmatrix} + \begin{bmatrix} 0 & -\omega_{en} & \omega_{eu} \\ \omega_{en} & 0 & -\omega_{nu} \\ -\omega_{eu} & \omega_{nu} & 0 \end{bmatrix}, \quad (3)$$

With the imaging geometry, the 3-D deformation can be derived by  $B \cdot A_{SM} \cdot X = D + \varepsilon$ , where  $B$  is formed with the imaging geometry,  $D$  is the observations vector,  $X$  consists of strain and 3-D deformation parameters,  $\varepsilon$  is the uncertainty of observations, and  $A_{SM}$  is the transform matrix formed by the position difference (J. Liu et al., 2019):

$$\begin{aligned} A_{SM}_{3N \times 12} &= \begin{bmatrix} A_{SM,1} & A_{SM,2} & A_{SM,3} \end{bmatrix}^T \\ &= \begin{bmatrix} 1 & 0 & 0 & \Delta p_e^1 & \Delta p_n^1 & \Delta p_u^1 & 0 & 0 & 0 & 0 & \Delta p_u^1 & -\Delta p_n^1 \\ \vdots & \vdots \\ 1 & 0 & 0 & \Delta p_e^N & \Delta p_n^N & \Delta p_u^N & 0 & 0 & 0 & 0 & \Delta p_u^N & -\Delta p_n^N \\ 0 & 1 & 0 & 0 & \Delta p_e^1 & 0 & \Delta p_n^1 & \Delta p_u^1 & 0 & -\Delta p_u^1 & 0 & \Delta p_e^1 \\ \vdots & \vdots \\ 0 & 1 & 0 & 0 & \Delta p_e^N & 0 & \Delta p_n^N & \Delta p_u^N & 0 & -\Delta p_u^N & 0 & \Delta p_e^N \\ 0 & 0 & 1 & 0 & 0 & \Delta p_e^1 & 0 & \Delta p_n^1 & \Delta p_u^1 & \Delta p_n^1 & \Delta p_e^1 & 0 \\ \vdots & \vdots \\ 0 & 0 & 1 & 0 & 0 & \Delta p_e^N & 0 & \Delta p_n^N & \Delta p_u^N & \Delta p_n^N & \Delta p_e^N & 0 \end{bmatrix} \end{aligned} \quad (4)$$

where the number in the subscript denotes the column and row indices of the corresponding matrix.

The implementation of the SM for deriving 3-D landslide movements could result in an ill-posed problem in the transform matrix  $B$  due to the influence of imaging geometry. To mitigate this limitation, we incorporate the SPF assumption into the SM. With the integration of the SPF assumption, the transform matrix is expected to be represented as

$$\begin{aligned} B_{SPF}_{4N \times 3N} &= \begin{bmatrix} (B_{SPF,1})^T & (B_{SPF,2})^T & (B_{SPF,3})^T & (B_{SPF,4})^T \end{bmatrix}^T \\ &= \begin{bmatrix} a_1^i \cdot I_N & b_1^i \cdot I_N & c_1^i \cdot I_N \\ a_2^i \cdot I_N & b_2^i \cdot I_N & c_2^i \cdot I_N \\ d_3^i \cdot I_N & e_3^i \cdot I_N & 0 \\ -\theta_e^i \cdot I_N & -\theta_n^i \cdot I_N & I_N \end{bmatrix} \end{aligned} \quad (5)$$

where  $I_N$  is the  $N$  identity matrix. On the basis of Equations 1 and 2, the 3-D landslide movements of a point  $P^0$  can then be derived by integrating the multi-source SAR-measured displacement of  $N$  surrounding points by

$$B_{SPF} \cdot A_{SM} \cdot X_{12 \times 1} = D_{SPFS} + \varepsilon_{SPFS}, \quad (6)$$

$$X_{12 \times 1} = \begin{bmatrix} v_e^0 & v_n^0 & v_u^0 & \zeta_{ee}^0 & \zeta_{en}^0 & \zeta_{eu}^0 & \zeta_{nn}^0 & \zeta_{nu}^0 & \zeta_{uu}^0 & \omega_{nu}^0 & \omega_{eu}^0 & \omega_{en}^0 \end{bmatrix}^T \quad (7)$$

where  $D_{SPFS}$  and  $\varepsilon_{SPFS}$  are the multi-source SAR measured displacement and its residuals at  $N$  surrounding points, respectively. The unknown vector  $X$  consists of 3-D deformation components to the point  $P^0$  and the corresponding strain components. It is important to note that upon integrating the SPF assumption, the virtual observations vector  $D_{VO}$  should be incorporated into the observations vector as

$$D_{SPFS} = \begin{bmatrix} v_1^1 \dots v_1^N & v_2^1 \dots v_2^N & v_3^1 \dots v_3^N & D_{VO} \end{bmatrix}^T \quad (8)$$

where  $D_{VO}$  is generated from a  $N \times 1$  matrix consisting of zero elements. The corresponding uncertainty matrix should be represented as

$$\varepsilon_{SPFS} = \begin{bmatrix} \varepsilon_{v1}^1 \dots \varepsilon_{v1}^N & \varepsilon_{v2}^1 \dots \varepsilon_{v2}^N & \varepsilon_{v3}^1 \dots \varepsilon_{v3}^N & \varepsilon_{VO} \end{bmatrix}^T \quad (9)$$

where  $\varepsilon_{vi}^N$  is the uncertainty of the corresponding measurement, and  $\varepsilon_{VO}$  is the uncertainty of virtual observation, which can be written as a  $N \times 1$  zero vector as well.

### 3.2.3. Final Solution

Considering that the multi-sources measurements are utilized in this study, the variance components estimator (VCE) is subsequently implemented to derive the precise weight and further optimize the 3-D landslide movements (J. Hu, LiZhi-Wei, et al., 2014). The VCE approach has been validated as a reliable method for deriving 3-D deformations from multi-sources SAR datasets. Because the measurements are derived from various measurements, the observations are classified into four groups: ALOS2-derived, Sentinel-1-derived, TanDEM-X-derived, and SPF-derived measurements. Then, we suppose that each of the initial weight matrices is equal to the identity matrix, that is,  $W_j = I_N$ , ( $j = 1, 2, 3$ ). The measurements and coefficient matrix of each group can be represented as  $D_j = \begin{bmatrix} v_j^1 & \dots & v_j^N \end{bmatrix}^T$ , and  $B_{SPFS,j} = B_{SPF,j} \cdot A_{SM}$ , respectively. Set that  $M_j = B_{SPFS,j}^T \cdot W_j \cdot B_{SPFS,j}$ ,  $F_j = B_{SPFS,j}^T \cdot W_j \cdot D_{SPFS,j}$ ,  $M = \sum_{j=1}^4 M_j$ , and  $F = \sum_{j=1}^4 F_j$ . Then, the unknown vector  $\hat{X}$  can be estimated by

$$\hat{X} = M^{-1} \cdot F \quad (10)$$

The relationship between the residuals of each group  $r_j = B_{SPFS,j} \cdot \hat{X} - D_{SPFS,j}$ . Note that the SPF assumption constitutes a virtual observation and as such, it does not include residuals (i.e.,  $r_{SPF} = 0$ ). Residuals were calculated only for the InSAR- and POT-derived measurements. Hence, variance components of InSAR- and POT-derived measurements  $\hat{\sigma}^2$  can be formed as

$$\hat{\sigma}^2 = \Gamma^{-1} W_r \quad (11)$$

with

$$\hat{\sigma}^2 = \begin{bmatrix} \hat{\sigma}_1^2 & \hat{\sigma}_2^2 & \hat{\sigma}_3^2 \end{bmatrix}^T \quad (12)$$

$$W_r = \begin{bmatrix} r_1^T \cdot W_1 \cdot r_1 & r_2^T \cdot W_2 \cdot r_2 & r_3^T \cdot W_3 \cdot r_3 \end{bmatrix}^T \quad (13)$$

$$\Gamma = \begin{bmatrix} N - 2\text{tr}(M^{-1}M_1) + \text{tr}(M^{-1}M_1)^2 & \text{tr}(M^{-1}M_1M^{-1}M_2) & \text{tr}(M^{-1}M_1M^{-1}M_3) \\ \text{tr}(M^{-1}M_2M^{-1}M_1) & N - 2\text{tr}(M^{-1}M_2) + \text{tr}(M^{-1}M_2)^2 & \text{tr}(M^{-1}M_2M^{-1}M_3) \\ \text{tr}(M^{-1}M_3M^{-1}M_1) & \text{tr}(M^{-1}M_3M^{-1}M_2) & N - 2\text{tr}(M^{-1}M_3) + \text{tr}(M^{-1}M_3)^2 \end{bmatrix}. \quad (14)$$

where  $\hat{\sigma}_1^2$ ,  $\hat{\sigma}_2^2$ , and  $\hat{\sigma}_3^2$  denote the variance components of ALOS2-derived, Sentinel-1-derived, and TanDEM-X-derived measurements, respectively. Subsequently, the variance components  $\hat{\sigma}^2$  can be utilized to improve the weight matrix of each group of observations

$$\hat{W}_1 = I_N, \hat{W}_2 = \frac{\hat{\sigma}_1^2}{\hat{\sigma}_2^2 \cdot W_2^{-1}}, \hat{W}_3 = \frac{\hat{\sigma}_1^2}{\hat{\sigma}_3^2 \cdot W_3^{-1}} \quad (15)$$

where  $\hat{W}_j$  is the improved weight matrix. These improved weight matrices are utilized in Equations 10, 11, and 15 to keep updating  $\hat{W}_j$  until the standard deviation of  $\hat{\sigma}^2$  is less than  $\mu^2$ .  $\mu$  is the convergence criteria determined according to the accuracy of the measurements and the elapsed time (J. Hu, LiZhi-Wei, et al., 2014). The updated weight matrix will improve  $M_j$  and  $F_j$ , which will be represented as  $\hat{M}_j$  and  $\hat{F}_j$ , respectively, during the iteration process. However, the part related to the SPF assumption is a virtual observation and should not be updated. For the iteration process and final solution,  $\hat{M}$  and  $\hat{F}$  should be expressed as

**Table 2**  
*RMSEs Between the Simulated and Estimated 3-D Movements*

Methods	RMSE		
	E-W (mm)	N-S (mm)	U-D (mm)
WLS	219.6	95.4	168.3
SPF	28.5	91.1	22.1
SPFS	8.9	15.6	5.2

$$\hat{M} = \sum_{j=1}^3 \hat{M}_j + M_{SPF} \quad (16)$$

$$= \sum_{j=1}^3 B_{SPFS,j}^T \cdot \hat{W}_j \cdot B_{SPFS,j} + B_{SPF}^T \cdot B_{SPF}$$

and

$$\hat{F} = \sum_{j=1}^3 \hat{F}_j + F_{SPF} \quad (17)$$

$$= \sum_{j=1}^3 B_{SPFS,j}^T \cdot \hat{W}_j \cdot D_{SPFS,j} + B_{SPF}^T \cdot D_{SPF}$$

$$= \sum_{j=1}^3 B_{SPFS,j}^T \cdot \hat{W}_j \cdot D_{SPFS,j}$$

With the updated  $\hat{M}$  and  $\hat{F}$ , the optimal 3-D landslide movements can be derived by Equation 10. Note that the SPFS method estimates the 3-D deformation of a target point by using the displacement-strain relationship of surrounding neighboring points. However, in the presence of discontinuities such as significant faults and cracks, the deformation on either side of such features may not follow this relationship, leading to unreliable 3-D deformation estimates. Hence, in order to obtain more reliable deformation estimates for a target point, it is necessary to use homogeneous neighboring points. The impact of cracks on the SPFS method does not only depend on their size, but also on the resolution, multi-look number, and filter parameter of the SAR observations. Cracks induced by an extensional or compressive zone would not significantly affect the model, and hence would not be considered in the SPFS method. The sensitivity of the boundary in the SPFS method is determined by the magnitude of deformation change on either side of it. Using manually delineated boundaries to constrain the results is recommended when significant deformation changes are observed in the SAR observations. These boundaries can then be employed to discard inhomogeneous pixels within the neighborhood when estimating the target 3-D deformations. In this study, we only observed a sharp crack in the toe of the Xinpu landslide complex. To ensure accurate estimation of the target 3-D deformations, we manually delineated the boundary of the landslide and its toe and utilized it to exclude inhomogeneous pixels within the neighborhood of the target point. It is worth noting that the deformation is derived pixel by pixel, and therefore, the submerged portion of the slope does not affect the acquisition of deformation.

## 4. Results

### 4.1. Algorithm Testing With the Synthetic Data

The advantage of synthetic datasets is that the estimated parameters are known and can be utilized for quantitative comparison of the performance of various methods. In this study, the 3-D movements of the landslide (Figures S2a–S2c in Supporting Information S1) are simulated by the SPF constraint. Three observations are then created by projecting the simulated 3-D movements to the LOS and AZI directions with the actual imaging geometric parameters of the data collected at the Xinpu landslide complex (Table 1). The decorrelation areas are extracted from the real datasets and added to the simulated POT observation (Figure S2c in Supporting Information S1). Considering the distinct accuracies of phase- and amplitude-based measurements, the Gaussian noises of different variances of 1.2, 0.8, and 9 cm<sup>2</sup> are added into the final observations with respect to the C-band-, L-band-derived LOS deformation, and POT-derived AZI deformation (Figures S2d–S2f in Supporting Information S1). Figures S2g–S2i in Supporting Information S1 shows that it is difficult to derive reliable 3-D movements by the conventional WLS method, and the results of the WLS method present severe noises, especially the movement of the up component, which is almost submerged by the noises. After implementing the SPF constraint, the reliability of 3-D movements is significantly improved, the spatial pattern of the up component is derived, and the noise is suppressed. Table 2 shows a quantitative comparison between various methods. It can be observed that the root-mean-square errors (RMSEs) of the east and up components estimated by SPF are obviously lower than those derived by the WLS method. Deformation dilution of precision (DDOP) is an indicator for assessing the reliability of derived 3-D deformation under a given configuration of SAR observations (J. Hu et al., 2021). The DDOPs of the WLS and SPF methods are 190.4 and 3.2, respectively, which means that the ill-posed condition is the main factor for reducing the reliability of the results derived by the WLS, and the SPF constraint can effectively solve this problem.

Although the SPF method can solve the ill-posed condition, the low SNR usually makes the POT measurement incomplete, which further affects the 3-D movements. Complete 3-D movements are critical for understanding the kinematics and mechanism of landslides (X. Hu et al., 2018). To overcome this limitation, the SPFS method is employed to derive the complete 3-D movements. It can be observed that the decorrelation area is recovered

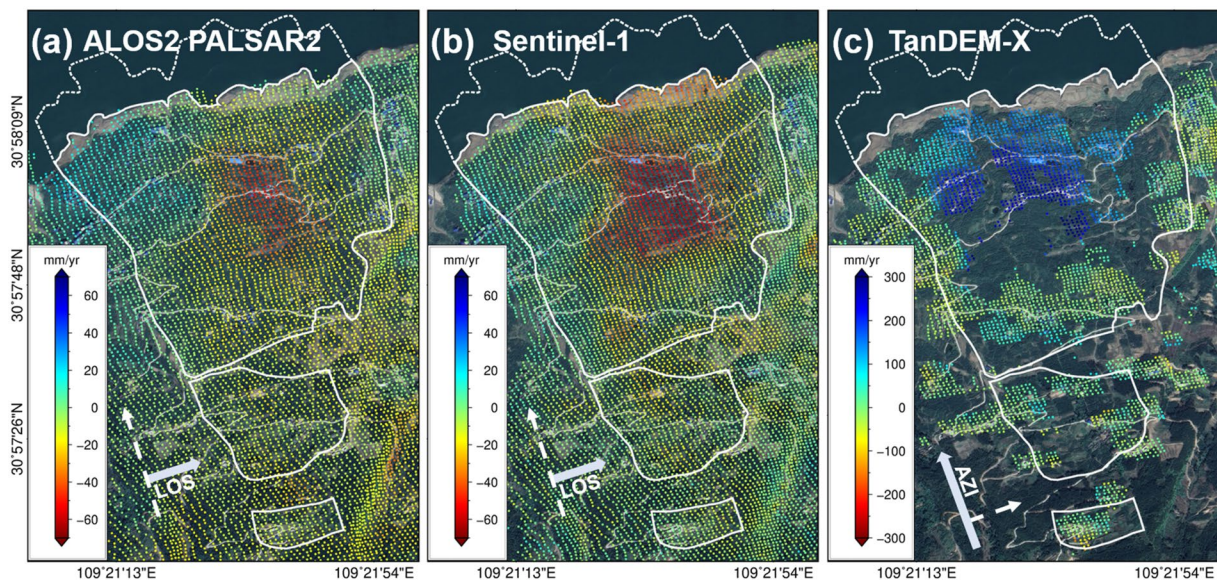


**Figure 3.** LOS/AZI landslide movements derived by (a) ALOS2 PALSAR2, (b) Sentinel-1A, and (c) TanDEM-X.

after implementing the SPFS method, and the derived 3-D movements present good agreement with the simulated ones (Figures S2m–S2o in Supporting Information S1). The RMSEs of the 3-D deformations derived by the SPFS method are all less than 2 cm.

#### 4.2. Applications to the Slow-Moving Xinpu Landslide Complex

The Xinpu landslide complex is a giant landslide in the TGR area, and the continuous movement and unexpected acceleration bring severe threats to residents (Figure S1 in Supporting Information S1). However, since the dense vegetation and the north-south aspect of the slope decrease the performance of InSAR, there are few related investigations of this landslide. In this study, multi-source SAR datasets are collected, and the optimized movements are then obtained by various methods based on the features of the corresponding datasets. L- and C-band-derived movements illustrate the spatially complete pattern, and the maximum LOS movement reaches approximately 65 mm/yr (Figures 3a and 3b). Differences in spatial patterns between ALOS-2 PALSAR2 and Sentinel-1 LOS measurements can be observed and may be attributed to several factors, including the significant difference in temporal resolution and the difference in local incident angle. Specifically, although the heading angle of these two datasets is similar, the different local incident angles can cause variations in the spatial pattern of the active deformation area (Y. Wang et al., 2020). Additionally, non-linear deformation is common in landslide movement, and the low temporal resolution of ALOS-2 PALSAR2 may potentially underestimate this type of movement (Wasowski & Bovenga, 2015).

With the high-resolution feature of TanDEM-X, we employed the pixel-offset SBAS algorithm (Casu et al., 2011) to obtain the azimuth movement of the Xinpu landslide. Note that the maximum LOS landslide movement only reaches approximately 65 mm/yr (Figures 3a and 3b). The accuracy of POT-derived measurements is around 1/10 pixels (i.e., 8.6 cm with TanDEM-X data) (L. Zhang et al., 2015). Therefore, it is difficult to obtain accurate LOS deformation with TanDEM-X datasets (Figure S3 in Supporting Information S1). As the Xinpu landslide complex is a north-oriented slope, the significant azimuth offset can be utilized to derive the 3-D movements. However, the dense vegetation reduces the SNR of the pixel offsets, and some of the offsets are unavailable (Figure 3c).

To derive the complete 3-D movement field of the Xinpu landslide complex, the proposed SPFS method is implemented, and the results are shown in Figure 4. For comparison, the 3-D movements of the Xinpu landslide complex are also estimated by the conventional WLS and SPF methods, respectively (Figure 4). It can be seen that it is difficult to obtain reliable 3-D movements by the WLS method. The errors of measurements are significantly magnified due to the ill-posed condition. After implementing the SPF constraint, the errors are quite suppressed, and reliable 3-D movements can be derived. However, the AZI observation is obtained from the X-band observation provided by the POT technique, and the areas with low SNR are masked. Therefore, the

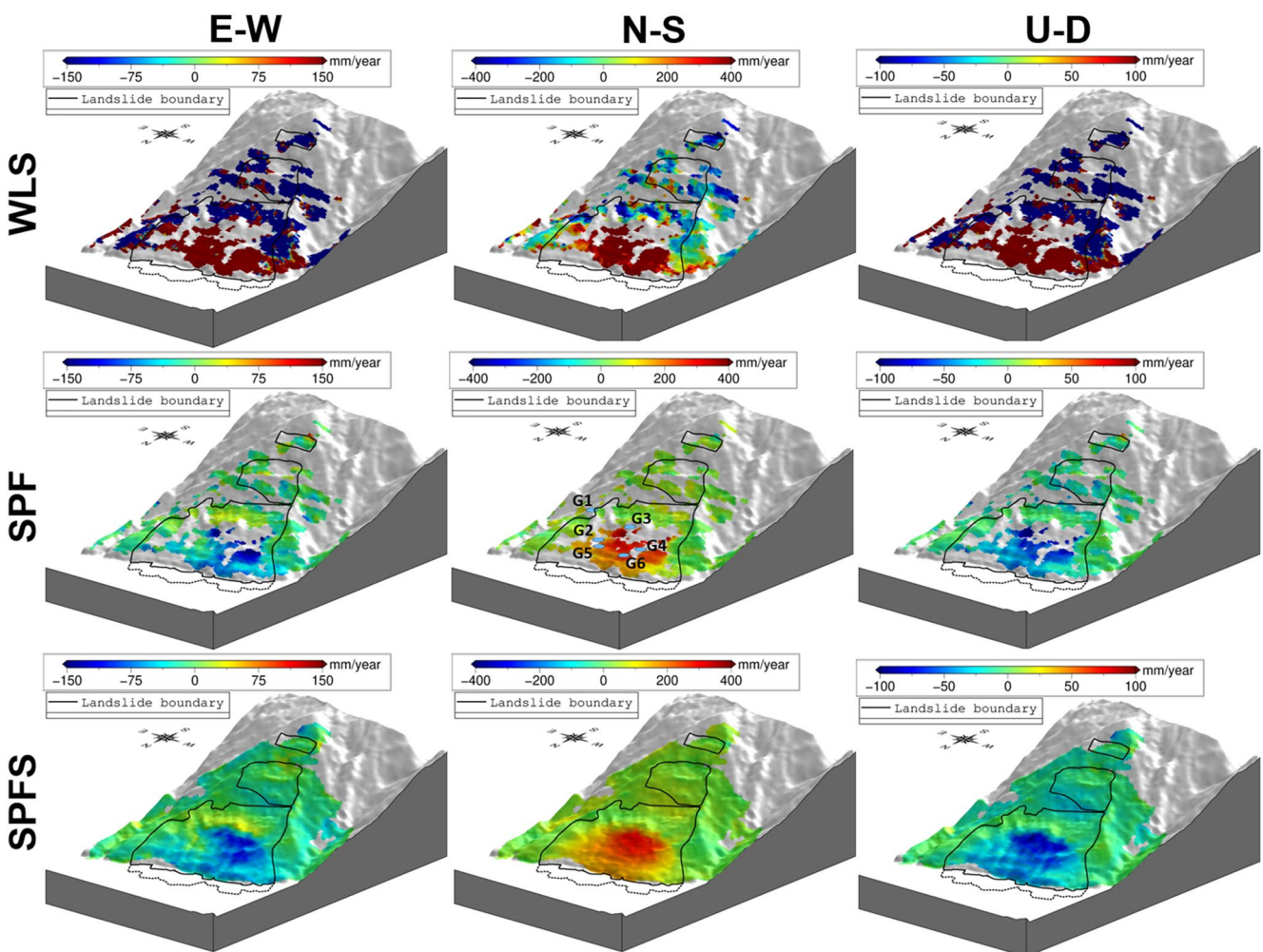


**Figure 4.** 3-D displacement of the Xinpu landslide complex derived by various methods. The blue circles in the central panel show the position of the GNSS stations.

SPF-derived 3-D movements of the Xinpu landslide complex are incomplete, which is unfavorable for understanding the kinematics of the Xinpu landslide complex. The SPFS method provides a solution to this problem. The spatially complete deformation field is derived after implementing the SPFS method (Figure 4).

By utilizing GNSS measurements, it is possible to derive 3-D time series deformation. There are several GNSS monitoring stations in the Xinpu landslide (as shown in Figure 1) (Q. Zhang et al., 2022b). This deformation can then be fitted to derive 3-D movement, as shown in Table S1 in Supporting Information S1. To quantitatively compare the performance of different methods, the RMSEs between the SAR- and GNSS-derived 3-D movements are calculated (see Table 3). Note that there are only two GNSS observations that can be utilized in the incomplete 3-D movements. It can be observed that there are significant differences between WLS- and GNSS-derived 3-D movements, and the corresponding RMSEs reach the decimeter to meter level, suggesting that the derived 3-D

movements are noisy. The centimeter-level RMSEs can be achieved by the SPF method, and the RMSEs in the east, north, and up components reach 34.1, 23.8, and 13.0 mm/yr, respectively. With respect to the results derived by the SPFS method, the RMSEs are further improved to 19.1, 15.7, and 6.7 mm/year in the east, north, and up components, respectively. The corresponding improvement reaches 44.0%, 34.0%, and 48.5% compared to those derived by the SPF method, which proves that the proposed SPFS can derive reliable 3-D movements.

The north component of movements presents the most significant deformation with a maximum value of approximately 332 mm/yr in the XET slope,

**Table 3**  
*The RMSEs Between the SAR- and GNSS-Measured 3-D Movements*

Methods	E-W (mm)		N-S (mm)		U-D (mm)	
	2 sites	5 sites	2 sites	5 sites	2 sites	5 sites
WLS	2,246.0	/	403.0	/	1,802.0	/
SPF	34.1	/	23.8	/	13.0	/
SPFS	19.1	15.0	15.7	35.6	6.7	12.8

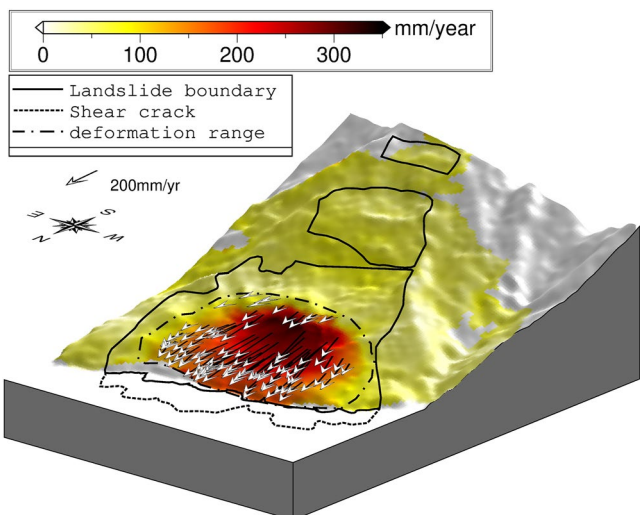


**Figure 5.** Amplitude and direction of movements in the Xinpu landslide complex. The amplitude of movements (background color) is derived from the 3-D movements. The white arrows indicate the direction of the movements.

and the upward and east components of movements reach approximately 105 and 129 mm/yr, respectively (Figure 4). According to the derived complete 3-D movements, the sliding direction of the Xinpu landslide complex is obtained and shown in Figure 5, indicating obvious north-westward movements. The amplitude of deformation can present the distribution of the movement (Zheng et al., 2021). XET slope is the primary deformation area with a maximum amplitude of approximately 370 mm/yr, and there are few significant deformations in the SET and DP slopes. Landslide geometry parameters can be characterized by the length, width, and aspect ratio, which are critical in inferring landslide propagation (L. Li et al., 2022). Compared to 1-D LOS deformation, 3-D movements are more comprehensive measurements to investigate landslides. Hence, we obtain the deformation range from the amplitude of movements (Figure 5), and the landslide geometry is then derived, in which the width and length of the Xinpu landslide are approximately 1.15 and 1.04 km, respectively, and the aspect ratio is approximately 0.90.

## 5. Discussions

### 5.1. The Performance of L-, C-, and X-Band SAR Datasets for Deriving the Time Series and 3-D Deformations of the Slow-Moving Landslide

The dense vegetation has pronounced effects on the performance of InSAR-derived movements, and the effects are different in various band InSAR measurements (Dong et al., 2018; Shi, Zhang, et al., 2017). In this study, the multi-source S AR observations are obtained simultaneously, which provides an opportunity to assess the resulting effects upon related InSAR measurements. Here, we intend to assess this effect by the multi-image phase coherence, which is an indicator to validate the reliability of InSAR-derived time series (Ferretti et al., 2000). Therefore, we estimate the corresponding multi-image phase coherence from six scenes of ALOS2 PALSAR2, 60 scenes of Sentinel-1A, and 12 scenes of TanDEM-X. Figure 6 presents the estimated results. The time series derived by ALOS2 PALSAR2 shows the highest multi-image phase coherence, followed by the C-band Sentinel-1A, and X-band TanDEM-X illustrates the lowest multi-image phase coherence. To quantitatively assess the results, the multi-image phase coherence within the boundaries of the Xinpu landslide complex is calculated, which are 0.76, 0.43, and 0.19 for the L-, C-, and X-band SAR data, respectively. It is impossible to derive a reliable phase from X-band TanDEM-X data in

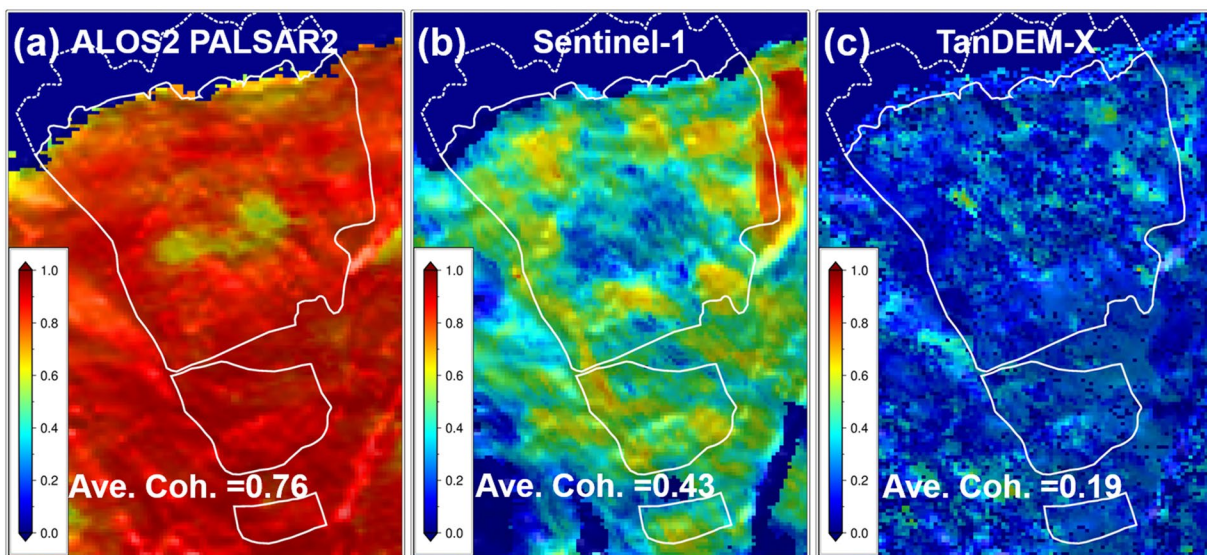


**Figure 6.** Comparison of multi-image phase coherence derived from (a) ALOS2 PALSAR2, (b) Sentinel-1, and (c) TanDEM-X.

vegetation areas. However, the TanDEM-X dataset has the highest spatial resolution among available space-borne SAR datasets in Xinpu. We implemented the POT technique to derive the azimuth deformation based on TanDEM-X's unique feature. The wavelength is not the only reason to reduce the reliability of X-band SAR data-derived time series, but also the temporal resolution. Although the revisit period of TanDEM-X can reach 11 days, it is difficult to obtain every 11-day scene in an unplanned region. However, Sentinel-1 can normally obtain each 12-day observation in any region, which is beneficial to derive a high multi-image phase coherence and reliable time series. Although only six scenes of L-band ALOS2 PALSAR2 are obtained during 2019–2022, the multi-image phase coherence is the highest, indicating the superiority of the long-wavelength SAR system. The forthcoming L-band LT-1 A/B (Jin et al., 2020) and NISAR (Simons et al., 2021) will provide a better repeat cycle, therefore, the performance of future L-band SAR in detecting potential landslides in dense vegetation areas is expected.

The forthcoming NISAR is a global-coverage satellite that will provide global L-band SAR observations for the general public (NISAR, 2018). All of the in-orbit space-borne SAR satellites work with the right-looking mode. To fill in coverage in the Antarctic area, NISAR will employ a unique left-looking mode for the mission (NISAR, 2018). In some areas, there are only ascending (or descending) observations (e.g., TGR areas), which brings significant uncertainties for deriving 3-D movements. The left-looking measurement provides an opportunity to enhance the performance of the derived 3-D movements (Wright, 2004). In this study, we obtained multi-band SAR observations, hence, the potential of NISAR measurements in estimating 3-D movements can be discussed with different combinations of SAR measurements. Cramér-Rao bound (CRB) is an indicator for assessing the theoretical accuracy of SAR/InSAR measurements (Bamler & Eineder, 2005; Delbridge et al., 2016). Here, the CRB of InSAR measurements is estimated with the multi-image phase coherence (as shown in Figure 7), and the CRB of POT measurement is estimated with the average cross-correlation (Bamler & Eineder, 2005). Due to that the coherence of the L-band NISAR measurements should be higher than that of ALOS2 PALSAR2, we utilized the multi-image phase coherence of ALOS2 PALSAR2 to estimate the CRB of NISAR. The CRB of 3-D movements  $\sigma_{CRB,3D}$  can be then derived by

$$\sigma_{CRB,3D} = [B^T \sigma_{obs}^{-1} B]^{-1} \quad (18)$$

where  $B$  and  $\sigma_{obs}$  are the transform matrix and observations' CRB, respectively.

The CRB derived by the WLS method presents significant uncertainty (Figures 7a–7c), especially in the east and north directions, and the CRB is larger than 300 mm/yr. The SPF assumption is necessary, after implementing the SPFS method, the CRB will significantly decrease (Figures 7d–7f). Similar imaging geometry is the main factor, and it is necessary to utilize some assumptions in such a combination of observations. We replace the ALOS2 PALSAR2 measurement with the ascending NISAR observation to estimate the CRB of real 3-D movement without the SPF assumption (Figures 7g–7i). The CRB is 0.6, 2.2, and 0.4 mm/yr in the east, north, and up directions, respectively, which are as good as those derived by the SPFS method. The CRB of 3-D movements with descending NISAR observations are also estimated (Figures 7j–7l), which present 18.3, 2.3, and 14.2 mm/yr in the east, north, and up components, respectively. Although the 3-D CRB with descending NISAR observations are worse than those with ascending observations, these results are still better than those derived with only right-looking observations (Figures 7j–7l). In particular, the CRB of the north component is not affected by the imaging track and presents a reliable result. The left-looking mode provides a special imaging geometry for deriving 3-D movements. When the left- and right-looking sensors flew in the same direction, the viewing angles were opposite, which would be very helpful for 3-D movement inversion (see Figures 7g–7i). Even when the left- and right-looking sensors fly in different directions, there are still differences in the viewing angles, which can assist in 3-D movement inversion (see Figures 7j–7l). In many cases, only ascending (or descending) track observations are available (e.g., the TGR area in this study). This limited selection will lead to significant uncertainty in deriving 3-D deformation. Combining the in-orbit right-looking SAR observations, the unique left-looking mode of NISAR will be helpful for deriving 3-D deformation, especially for some areas with only ascending (or descending) tracks, the 3-D deformations can be derived without any assumption.

To achieve wide coverage with high azimuth resolution, NISAR will utilize the SweepSAR technique (NISAR, 2018), which is different from the TOPSAR mode (De Zan & Guarnieri, 2006). The higher resolution observation from SweepSAR can enhance the performance of the POT technique and improve the 3-D inversion results. Additionally, NISAR's dual-frequency observation is a unique feature that can estimate the ionospheric phase and improve the accuracy of the azimuth offset estimation (Rosen et al., 2010). However, it should be noted that the S-band data, which can be used for ionospheric correction, will not be available globally (NISAR, 2018), and its coverage will be limited in some regions. To address this limitation, NISAR will provide additional 5 MHz sub-band data to estimate the ionospheric phase. By using the 5 MHz iono band or S-band data, the ionospheric

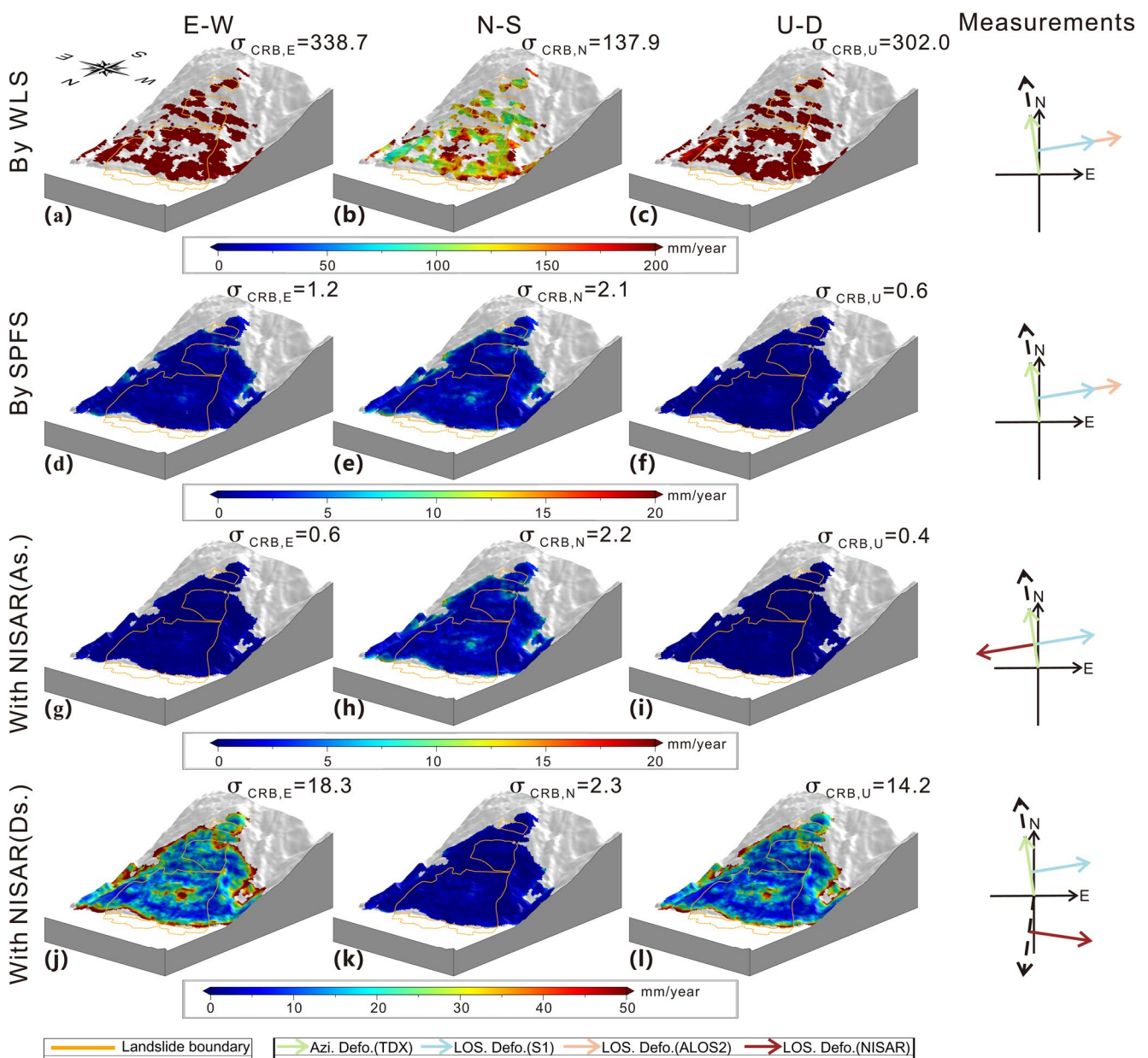


**Figure 7.** Comparison of Cramér-Rao bounds (CRB) for 3-D movements using different methods and measurements. (a)–(f) show the CRB using the WLS and SPFS methods with multi-source measurement. (g)–(l) show the CRB using Sentinel-1, TanDEM-X, and ascending/descending NISAR measurements without assumption.

phase screen can be derived (NISAR, 2018), which presents an opportunity to increase the accuracy of both the azimuth offset and 3-D deformations.

## 5.2. The Inferred Depth of the Xinpu Landslide Complex

The volume and depth of landslides are fundamental parameters for understanding the mechanism of landslides and assessing the risks (X. Hu et al., 2019; X. Hu et al., 2018; Shi et al., 2021). The Xinpu landslide complex is a deep-seated slow-moving landslide. Because of the large depth and wide area, the cost of deriving the volume and depth by conventional methods (e.g., borehole drilling or tunnel excavation) is enormous. In past decades, remote sensing has provided a low-cost method to derive the depth and volume through some models, for instance, the depth-area and volume-area relationships (Cohen-Waeber et al., 2018), the vector inclination method (Shi et al., 2021), and the law of mass conservations (X. Hu et al., 2018), in which the law of mass conservation can derive the pixel-by-pixel depth and thus the basal geometry. The conservation of mass gives an equation of

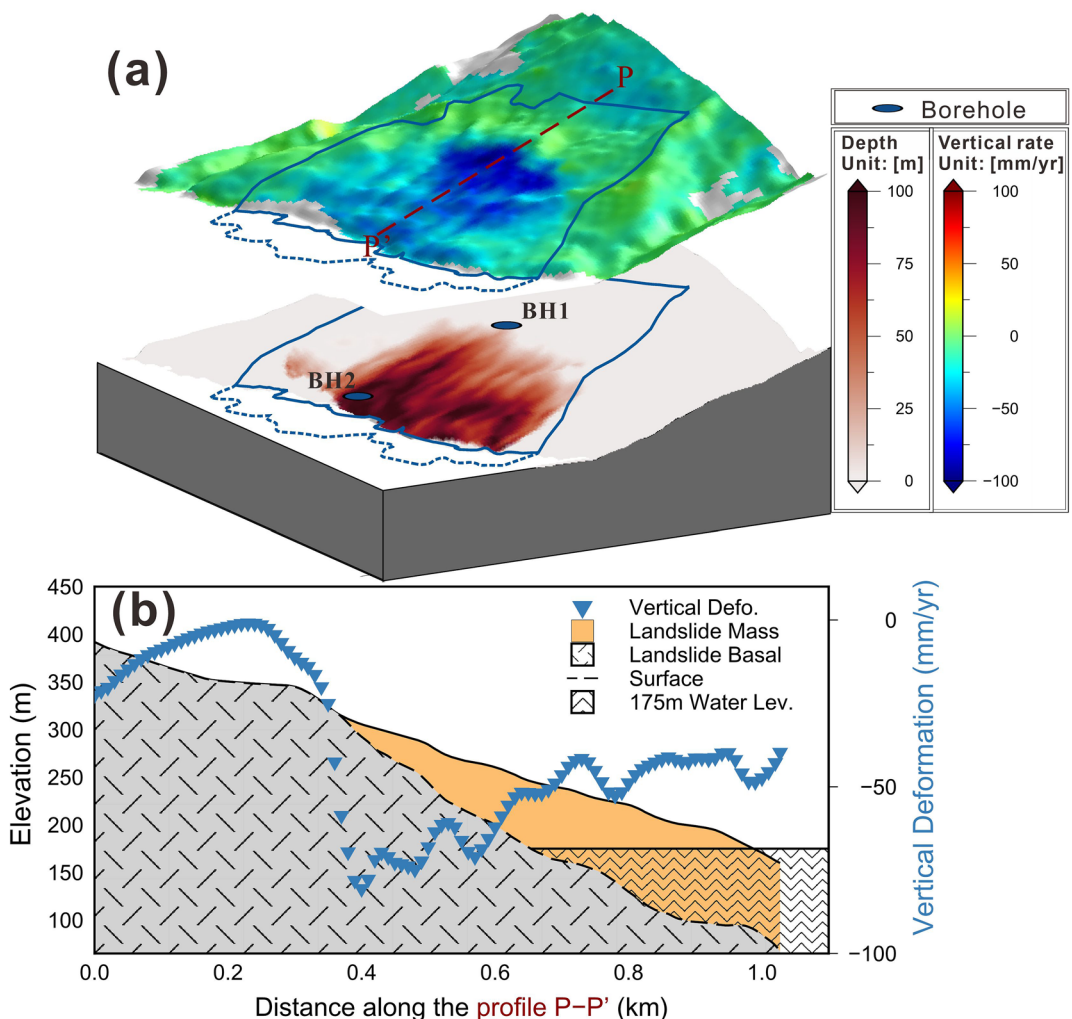


**Figure 8.** (a) The inferred depth of the Xinpu landslide complex, derived by the inversion of the 3-D movements. The slope in the top layer is the vertical movement, and that in the bottom layer is the geometry of the basal surface. (b) The vertical deformation, surface topography, derived thickness, and basal surface along profile P-P'.

the mathematical relation between mass flux divergence and the rate of thickness change (Booth et al., 2013). The complete 3-D deformation field is the necessary parameter for deriving the depth. However, a portion of the landslide is submerged in water, which poses a challenge for depth inversion. To address this limitation, we utilized the 3-D movements derived from multi-source SAR observations over the slope above the water and Equation S2.3 in Supporting Information S1 as well as the boundary of landslide to estimate the landslide deformation beneath the water using a SM. Subsequently, we determined the depth and volume of the Xinpu landslide complex by applying the law of mass conservation (see Text S2 in Supporting Information S1).

Figure 8a illustrates the depth and basal geometry of the Xinpu landslide complex. To validate the results, the stratum derived by the drilling core is adopted for comparison with the derived thickness. The stratum result of BH1 shows that the depth of landslide is 26.4 m, while the estimated depth is 25.9 m, a difference of approximately 0.5 m is presented. A second borehole (BH2) was drilled to a depth of 36 m, which did not reach the basal plane of the landslide, suggesting that the actual depth is greater than 36 m. Our estimate of the depth at BH2 is 95.7 m, which exceeds the observed depth of 36 m. While we set the uncertainty of the thickness to  $\pm 0.5$  m in this study, it is important to note that this value was based on limited in situ measurements. Further evaluation of the results will be necessary as additional measurements become available. As shown in Figure 8a, the average depth is  $47.8 \pm 0.5$  m, and the maximum depth can reach  $100 \pm 0.5$  m, which is located near the toe of the XET slope. An apparent transport zone can be observed between the middle section and the toe of the XET slope, extending

to the areas under the river. According to the derived depth, the estimated volume is  $3.52 \times 10^7 \text{ m}^3$ , in general matching the previous in situ investigation of about  $3 \times 10^7 \text{ m}^3$  based on a few boreholes in the landslide. To further elucidate the relationship between deformation and basal geometry, we derive the vertical deformation, depth, and basal geometry along profile P-P' (Figure 8b). Since there is no mass compensation in the part of the thinnest landslide mass, the mass of this part is thinning. A significant acceleration of vertical deformation can be observed in the thinnest part, and the maximum value of vertical deformation reaches  $-80.6 \text{ mm/yr}$ . Such a phenomenon usually leads to cracks, which is also supported by the in-situ investigation (as shown in Figure S1 in Supporting Information S1). Instead, as the mass compensation moves from the rear section of the slope, the vertical deformation decreases from  $80.6 \text{ mm/yr}$  to approximately  $50.0 \text{ mm/yr}$ . Note that the maximal water level of 175 m submerges a part of the landslide basal (Figure 8b). However, the vertical deformation does not quite suffer from the fluctuating water level. According to the previous work about the geohazards of TGR areas, most landslides have been impacted by fluctuations in the water level since the impoundage from 145 to 175 m in 2008 (S. Li et al., 2018). For example, since the reservoir water level decreased by approximately 25 m from November 2008 to June 2009, a significant movement of approximately 0.6 m was detected in the Shuping landslide (Shi et al., 2015), and similar landslide movement behavior was also found in the Huangtupo landslide (P. Liu et al., 2013). The water pressure difference between the inside and outside of the landslide is the primary factor for landslide acceleration (Paronuzzi et al., 2013). The inward pressure difference induced by the impoundment helps to enhance the stability of the landslide, instead, the outward pressure difference caused by the reservoir discharge can incline the threats of slope failure (Paronuzzi et al., 2013; Shi et al., 2015). Rather than the 8-month discharge operation in 2008–2009, it can be observed that the discharge operation only lasted for 3–4 months during 2019–2022. Then, the reservoir will turn into an impoundment operation (Figure S4 in Supporting Information S1). Hence, we consider a negligible influence of the water level due to hypothesize that the short-term discharge operation and the immediate impoundment operation contribute to decreasing the influence of the water level in the Xinpu landslide complex.

### 5.3. The Correlation Between the InSAR-Derived Movement and Triggers During 2016–2022

Reservoir bank slopes are usually impacted by the joint effects of precipitation and the fluctuation of water level and present significant accelerated movements during the wet season (e.g., the Shuping landslide (Shi et al., 2015), Huangtupo landslide (Tomás et al., 2014), and Qianjiangping landslide (F.-W. Wang et al., 2004)). Deriving the relationship between deformation and triggers helps us better understand the landslide mechanism. Thanks to the development of the InSAR technique, there are a tremendous number of available SAR archives that can help derive the evolution of landslide movements. In this study, we obtained more than 160 scenes of the Sentinel-1 archive to obtain the movement history of the Xinpu landslide complex during 2016–2022. Similar to most landslide reservoir areas (Shi et al., 2015, 2021), the cumulative movements of the Xinpu landslide complex present a pronounced step pattern (Figure 9a), and accelerated deformation can be observed in each wet season, therefore, the rainfall and the fluctuation of the water level should be considered the main triggers of the Xinpu landslide complex. To better understand the effects of various triggers, we implement the ICA approach (Chaussard et al., 2017; Cohen-Waeber et al., 2018) to divide the effects from the cumulative deformation. Figure S4 in Supporting Information S1 shows the scores and the eigenvectors derived by the ICA approach, which indicate the weight and the temporal pattern of the corresponding triggers, respectively. The score of IC1 is mainly found in the central section of the XET slope (Figure S4b in Supporting Information S1). In contrast, the score of IC2 concentrates on the toe of the XET slope (Figure S4c in Supporting Information S1). The influence of the water level is usually concentrated in the toe of the landslide (Shi et al., 2015; Tantianuparp et al., 2013), therefore, IC2 may indicate the water level-induced component, and IC1 could be affected by rainfall. From the temporal patterns of each component, it can be seen that the eigenvector of IC2 presents the apparent cyclical movement that matches the fluctuation of the water level (Figure S4a in Supporting Information S1). The eigenvector of IC1 only shows a significant acceleration in 2017, 2020, and 2021. This also proves that IC1 and IC2 are the components impacted by precipitation and water level, respectively. The ICA-derived results illustrate slight effects of the water level on the Xinpu landslide complex, which is consistent with the findings in Section 5.2. Instead, precipitation is the main trigger of the movement of the Xinpu landslide complex, and dense heavy rainfall could threaten the safety of the Xinpu landslide complex.

Rainwater recharge increases the subsurface pore-water pressure and induces accelerated movement. By the 1-D diffusion model, the transient pore-water pressure variation can be characterized by the daily precipitation record

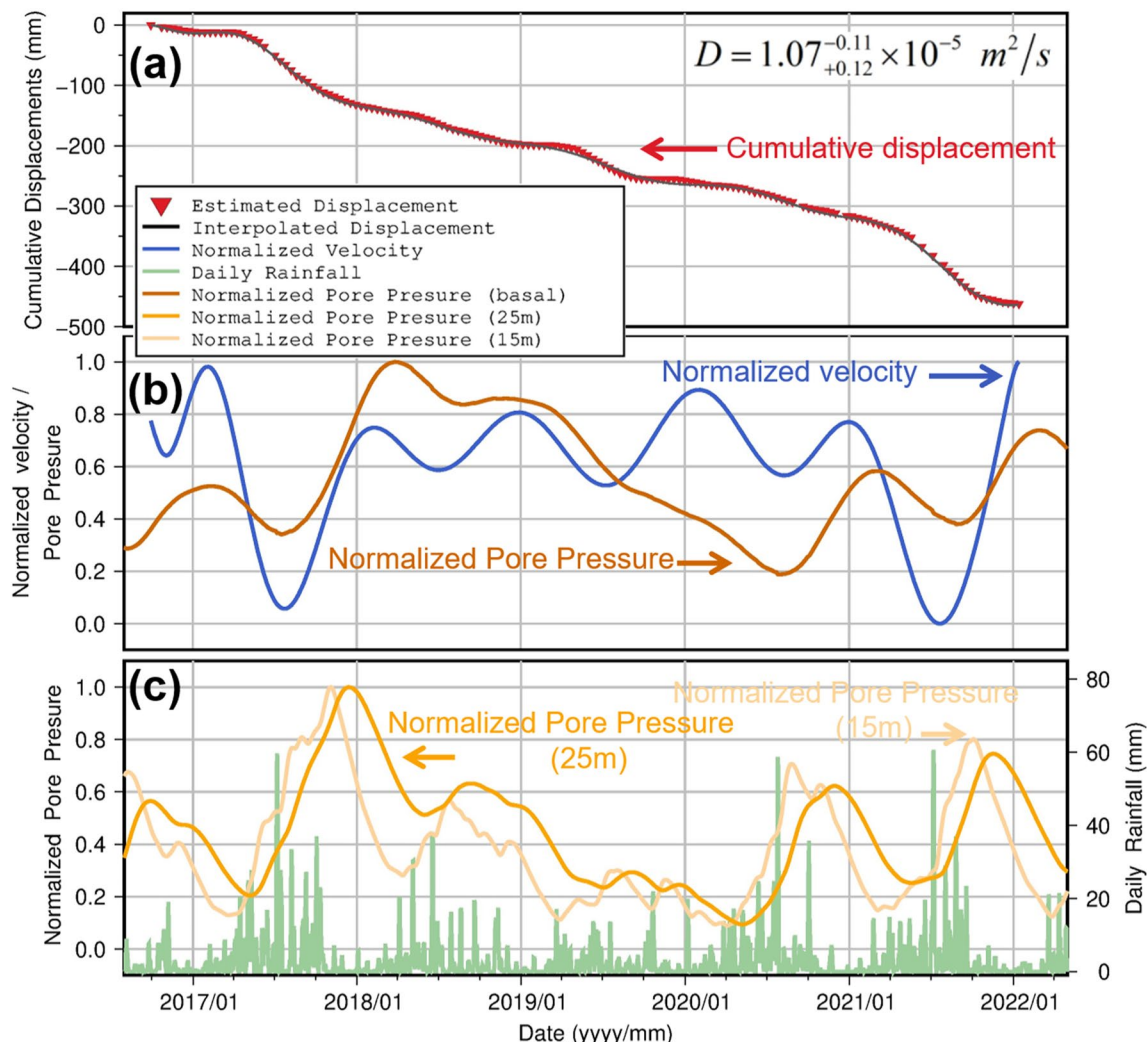


**Figure 9.** Landslide cumulative displacement, velocity, precipitation, and inferred pore pressure. (a) The cumulative displacement of the Xinpu landslide complex during 2016–2022.  $D$  is the inferred hydraulic diffusivity. (b) The normalized velocity and the pore pressure derived by the 1-D diffusion model. (c) The precipitation and pore pressure at different depths.

(Handwerger et al., 2016). The pore-water pressure changes during 2016–2022 are derived by the 1-D diffusion model to quantitatively assess the impacts of rainfall in modulating the landslide movement. The effective hydraulic diffusivity is the critical parameter to derive the pore-water changes and can be estimated from the best correlation between the simulated pore pressure at a given depth and the derived time-series landslide movement rate (see Text S3 in Supporting Information S1). Note that the inferred depth obtained in the last section is helpful for decreasing the search range of estimating the effective hydraulic diffusivity and increasing the computational efficiency. For the deep-seated slow-moving landslide, the effective hydraulic diffusivity is in the range from  $10^{-6}$  to  $10^{-4} \text{ m}^2/\text{s}$  (X. Hu et al., 2019), for example, the diffusivity of the Cleveland Corral landslide is  $5 \times 10^{-6} \text{ m}^2/\text{s}$  (Kang et al., 2021), and that of the Monroe landslide is  $7.94 \times 10^{-5} \text{ m}^2/\text{s}$ . In this study, we set  $\pm 1.0 \text{ m}$  as the windows of derived depth to explore the best-fit value, and 0.2% of the minimum residual is considered as solutions (see Text S3 in Supporting Information S1). The characteristic diffusivity is constrained to be  $1.07^{-0.11}_{+0.12} \times 10^{-5} \text{ m}^2/\text{s}$  (with a 95% confidence bound) for the observation between 2016 and 2022. Then, the simulated pore-water pressure change at the basal is calculated based on the estimated diffusivity using a 1-D diffusivity model. First, we use the derived characteristic diffusivity to calculate  $h(t)$ , and then pore-water pressure at the ground surface,  $p(t, z = 0)$ , is derived using Equation (S3.2 in Supporting Information S1). As in-situ pore water pressure measurements were not available, we used a normalization approach to account for daily precipitation data and eliminate the impact of infiltration scaling factor. Consequently, the derived pore-water pressure is also normalized to

the range of [0, 1]. Since the pore-water pressure can be expressed as the convolution of  $h(t)$  and  $p(t, z = 0)$ , we use Fourier transforms to convert  $h(t)$  and  $p(t, z = 0)$  from the time domain to the frequency domain. Finally, the pore-water pressure is obtained using an inverse Fourier transform with Equation (S3.6 in Supporting Information S1). As shown in Figure 9b, although the velocities of movement increased in each wet season, significant increases in pore-water pressure at the basal were only observed in 2017, 2020, and 2021 (Figure 9b, the brown line). The dense heavy rainfall is the leading cause of the increased pore-water pressure, and it can be observed in the precipitation record that there was heavy rainfall of more than 50 mm/d in 2017, 2020, and 2021 (Figure 9c). In accordance with the present findings, the previous in-situ investigation shows that the landslide movements significantly damaged the local infrastructure (Figure S1c in Supporting Information S1) during the wet season in 2020 and 2021. Hence, more attention should be given to the impacts of precipitation.

Using the derived effective diffusivity, we can also derive the pore water pressure at a given depth. Here, the subsurface pore-water pressure changes at depths of 15 and 25 m are further derived by the 1-D diffusion model (i.e., Equation (S3.3)–Equation (S3.6) in Supporting Information S1), respectively. As illustrated in Figure 9c, the time lag between the pore-water pressure changes at different depths can be observed. The peak of the pore-water pressure at a depth of 15 m occurs in November, while that at a depth of 25 m reaches its peak in December. Similarly, the pore-water pressure at the basal plane reaches the peak much later than at depths of 15 and 25 m. In addition, the sensitivity of pore-water pressure to precipitation is different at various depths. The pore-water pressure increased at depths of 15 and 25 m during the wet season of 2018, whereas few increases can be observed in the pore-water pressure changes at the basal plane. Therefore, for the clay-rich slow-moving landslide in the TGR area with a shallower basal plane than the Xinpu landslide complex, the effects of rainfall could be more prominent, in which the sensitivity to precipitation could be strong, and the response time may be shorter.

## 6. Conclusions

Our study presents a surface parallel flow constrained strain (SPFS) model for deriving the complete 3-D landslide movements by integrating multi-source SAR observations. The proposed method overcomes the ill-posed condition caused by the similarity of the imaging geometries and retrieves the complete 3-D movement field with higher accuracy than conventional methods. Our assessment of the method on synthetic and real datasets shows its effectiveness and potential for future applications.

Furthermore, we assessed the performance of various frequency SAR datasets in deriving time-series deformation, highlighting the advantages of L-band observations and the importance of regular short revisits in vegetated areas. We also explored the potential of left-looking NISAR observations in estimating reliable 3-D movements and found it to be a massive improvement over other datasets, making the forthcoming NISAR datasets more attractive for landslide investigations.

We obtained 3-D movements of the Xinpu landslide complex in the TGR area via the SPFS method using L-band ALOS2 PALSAR2, C-band Sentinel-1, and X-band TanDEM-X datasets from 2019 to 2022. Our analysis of these movements provided valuable landslide metrics, including geometry parameters, movement patterns, thickness, and hydraulic diffusivity. Our findings indicate that water level fluctuations had a minimal effect on the landslide, but pore-water pressure changes at varying depths showed clear rainfall effects. Additionally, we observed a significant transport tunnel from the middle to the submerged region based on the derived basal geometry. In conclusion, our study provides novel insights into the Xinpu landslide complex.

## Data Availability Statement

The TanDEM-X datasets are provided by the Deutsche Zentrum für Luft-und Raumfahrt (DLR) under the general AO project (No. MTH3631) and can be found on the EOWEB Geoportal website (<https://eoweb.dlr.de/egp/>). The ALOS-2 PALSAR2 datasets are provided by the Japan Aerospace Exploration Agency (JAXA) and can be found on the G-Portal website (<https://gportal.jaxa.jp/>). The Sentinel-1 images and Copernicus DEM are copyrighted by the European Space Agency (ESA) and are freely downloaded from the <https://search.asf.alaska.edu/> and <https://opentopography.org/>, respectively. The GNSS raw observations and derived three-dimensional deformation can be found on the ChinaGEOSS Data Sharing Network of the National Earth Observation Data Center (<https://www.chinageoss.cn/datasharing/datasetDetails/629824bc35d79468ce23849d> & <https://www.chinageoss.cn/datasharing/datasetDetails/62982b8335d79468ce2384b2>). The precipitation records are available

## Acknowledgments

We thank Editor Paul Tregoning, Associate Editor Lujia Feng, and anonymous reviewers for their insightful comments. We thank Prof. Honghu Zhu of Nanjing University for providing the borehole data, Prof. Guanwen Huang of Chang'an University for providing the GNSS observations, Dr. Ya Kang of Nanjing University of Posts and Telecommunications for providing helpful comments in the pore-water pressure modeling, and Mr. Mingjun Hu of Chongqing 208 Geo-environmental Research Institute Co. Ltd for providing the water level records and basic information of the Xinpu landslide complex. The research was supported by the National Natural Science Foundation of China (42030112), the Natural Science Foundation of Hunan Province (2022JJ30031), the Science and Technology Innovation Program of Hunan Province (2022RC3042), the Project of Innovation-driven Plan of Central South University (2019CX007), and the Fundamental Research Funds for the Central Universities of Central South University (2019zzts298).

at <https://www.ncei.noaa.gov/maps/daily/>. Several figures were plotted using Generic Mapping Tools (GMT) software.

## References

- Bamler, R., & Eineder, M. (2005). Accuracy of differential shift estimation by correlation and split-bandwidth interferometry for wideband and delta-k SAR systems. *IEEE Geoscience and Remote Sensing Letters*, 2(2), 151–155. <https://doi.org/10.1109/lgrs.2004.843203>
- Bechor, N. B. D., & Zebker, H. A. (2006). Measuring two-dimensional movements using a single InSAR pair. *Geophysical Research Letters*, 33(16). <https://doi.org/10.1029/2006gl026883>
- Berardino, P., Fornaro, G., Lanari, R., & Sansosti, E. (2002). A new algorithm for surface deformation monitoring based on small baseline differential SAR interferograms. *IEEE Transactions on Geoscience and Remote Sensing*, 40(11), 2375–2383. <https://doi.org/10.1109/tgrs.2002.803792>
- Booth, A. M., Lamb, M. P., Avouac, J.-P., & Delacourt, C. (2013). Landslide velocity, thickness, and rheology from remote sensing: La Clapière landslide, France. *Geophysical Research Letters*, 40(16), 4299–4304. <https://doi.org/10.1029/grl.50828>
- Casu, F., Manconi, A., Pepe, A., & Lanari, R. (2011). Deformation time-series generation in areas characterized by large displacement dynamics: The SAR amplitude pixel-offset SBAS technique. *IEEE Transactions on Geoscience and Remote Sensing*, 49(7), 2752–2763. <https://doi.org/10.1109/tgrs.2010.2104325>
- Chaussard, E., Milillo, P., Bürgmann, R., Perissin, D., Fielding, E. J., & Baker, B. (2017). Remote sensing of ground deformation for monitoring groundwater management practices: Application to the Santa Clara Valley during the 2012–2015 California drought. *Journal of Geophysical Research: Solid Earth*, 122(10), 8566–8582. <https://doi.org/10.1002/2017jb014676>
- Cohen-Waeber, J., Bürgmann, R., Chaussard, E., Giannico, C., & Ferretti, A. (2018). Spatiotemporal patterns of precipitation-modulated landslide deformation from independent component analysis of InSAR time series. *Geophysical Research Letters*, 45(4), 1878–1887. <https://doi.org/10.1002/2017gl075950>
- Delbridge, B. G., Bürgmann, R., Fielding, E., Hensley, S., & Schulz, W. H. (2016). Three-dimensional surface deformation derived from airborne interferometric UAVSAR: Application to the slumgullion landslide. *Journal of Geophysical Research: Solid Earth*, 121(5), 3951–3977. <https://doi.org/10.1002/2015jb012559>
- De Zan, F., & Guarneri, A. M. (2006). Topsar: Terrain observation by progressive scans. *IEEE Transactions on Geoscience and Remote Sensing*, 44(9), 2352–2360. <https://doi.org/10.1109/tgrs.2006.873853>
- Dong, J., Zhang, L., Tang, M., Liao, M., Xu, Q., Gong, J., & Ao, M. (2018). Mapping landslide surface displacements with time series SAR interferometry by combining persistent and distributed scatterers: A case study of Jiaju landslide in Danba, China. *Remote Sensing of Environment*, 205, 180–198. <https://doi.org/10.1016/j.rse.2017.11.022>
- Ferretti, A., Prati, C., & Rocca, F. (2000). Nonlinear subsidence rate estimation using permanent scatterers in differential SAR interferometry. *IEEE Transactions on Geoscience and Remote Sensing*, 38(5), 2202–2212. <https://doi.org/10.1109/36.868878>
- Handwerger, A. L., Huang, M. H., Fielding, E. J., Booth, A. M., & Bürgmann, R. (2019). A shift from drought to extreme rainfall drives a stable landslide to catastrophic failure. *Scientific Reports*, 9(1), 1569. <https://doi.org/10.1038/s41598-018-38300-0>
- Handwerger, A. L., Rempel, A. W., Skarbek, R. M., Roering, J. J., & Hilsley, G. E. (2016). Rate-weakening friction characterizes both slow sliding and catastrophic failure of landslides. *Proc Natl Acad Sci U S A*, 113(37), 10281–10286. <https://doi.org/10.1073/pnas.1607009113>
- Hu, J., Ding, X.-L., Zhang, L., Sun, Q., Li, Z.-W., Zhu, J.-J., & Lu, Z. (2017). Estimation of 3-D surface displacement based on InSAR and deformation modeling. *IEEE Transactions on Geoscience and Remote Sensing*, 55(4), 2007–2016. <https://doi.org/10.1109/tgrs.2016.2634087>
- Hu, J., Li, Z., Ding, X., Zhu, J., Zhang, L., & Sun, Q. (2014). Resolving three-dimensional surface displacements from InSAR measurements: A review. *Earth-Science Reviews*, 133, 1–17. <https://doi.org/10.1016/j.earscirev.2014.02.005>
- Hu, J., Liu, J., Li, Z., Zhu, J., Wu, L., Sun, Q., & Wu, W. (2021). Estimating three-dimensional coseismic deformations with the SM-VCE method based on heterogeneous SAR observations: Selection of homogeneous points and analysis of observation combinations. *Remote Sensing of Environment*, 255(15). <https://doi.org/10.1016/j.rse.2021.112298>
- Hu, J., LiZhi-Wei, L., Jia, Z., Lei, L., Ding, X.-L., Xiao-Li, J.-J., et al. (2014a). 3-D movement mapping of the alpine glacier in Qinghai-Tibetan Plateau by integrating D-InSAR, MAI and Offset-Tracking: Case study of the Dongkemadi Glacier. *Global and Planetary Change*, 118, 62–68. <https://doi.org/10.1016/j.gloplacha.2014.04.002>
- Hu, X., Bürgmann, R., Lu, Z., Handwerger, A. L., Wang, T., & Miao, R. (2019). Mobility, thickness, and hydraulic diffusivity of the slow-moving monroe landslide in California revealed by L-band satellite radar interferometry. *Journal of Geophysical Research: Solid Earth*, 124(7), 7504–7518. <https://doi.org/10.1029/2019jb017560>
- Hu, X., Lu, Z., Pierson, T. C., Kramer, R., & George, D. L. (2018). Combining InSAR and GPS to determine transient movement and thickness of a seasonally active low-gradient translational landslide. *Geophysical Research Letters*, 45(3), 1453–1462. <https://doi.org/10.1029/2017gl076623>
- Huang, B., Yin, Y., Liu, G., Wang, S., Chen, X., & Huo, Z. (2012). Analysis of waves generated by Gongjiafang landslide in Wu Gorge, three Gorges reservoir, on November 23, 2008. *Landslides*, 9(3), 395–405. <https://doi.org/10.1007/s10346-012-0331-y>
- Huang, G., Wang, J., Du, Y., Bai, Z., & Wang, D. (2021). Time-delay analysis and prediction of landslide considering precipitation and reservoir water level - a case study of Xinpu landslide in Three Gorges Reservoir area, China. *Journal of Earth Sciences and Environment*, 43(3), 621–631. <https://doi.org/10.19814/j.jese.2021.01019>
- Jin, G., Kaiyu, L., Dacheng, D., Liang, D., Zhang, H., Ou, N., et al. (2020). An advanced phase synchronization scheme for LT-1. *IEEE Transactions on Geoscience and Remote Sensing*, 58(3), 1735–1746. <https://doi.org/10.1109/tgrs.2019.2948219>
- Joughin, I. R., Kwok, R., & Fahnestock, M. A. (1998). Interferometric estimation of three-dimensional ice-flow using ascending and descending passes. *IEEE Transactions on Geoscience and Remote Sensing*, 36(1), 25–37. <https://doi.org/10.1109/36.655315>
- Kang, Y., Lu, Z., Zhong, Z., Chaoying, Y., Xu, J.-w., Yuankun, A. J., et al. (2021). InSAR monitoring of creeping landslides in mountainous regions: A case study in Eldorado National forest, California. *Remote Sensing of Environment*, 258, 112400. <https://doi.org/10.1016/j.rse.2021.112400>
- Lacroix, P., Handwerger, A. L., & Bièvre, G. (2020). Life and death of slow-moving landslides. *Nature Reviews Earth & Environment*, 1(8), 404–419. <https://doi.org/10.1038/s43017-020-0072-8>
- Li, C., Fu, Z., Wang, Y., Tang, H., Yan, J., Gong, W., et al. (2019). Susceptibility of reservoir-induced landslides and strategies for increasing the slope stability in the Three Gorges Reservoir Area: Zigui Basin as an example. *Engineering Geology*, 261, 105279. <https://doi.org/10.1016/j.engeo.2019.105279>
- Li, L., Lan, H., Strom, A., & Macciotta, R. (2022). Landslide length, width, and aspect ratio: Path-dependent measurement and a revisit of nomenclature. *Landslides*, 19, 3009–3029. <https://doi.org/10.1007/s10346-022-01935-2>

- Li, S., Qiang, Q., Tang, M., Iqbal, J., Javed, L., Zhu, X., et al. (2018). Characterizing the spatial distribution and fundamental controls of landslides in the Three Gorges Reservoir area, China. *Bulletin of Engineering Geology and the Environment*, 78(6), 4275–4290. <https://doi.org/10.1007/s10064-018-1404-5>
- Liu, J., Hu, J., Xu, W., Li, Z., Zhu, J., Ding, X., & Zhang, L. (2019). Complete three-dimensional coseismic deformation field of the 2016 Central Tottori earthquake by integrating left-and right-looking InSAR observations with the improved SM-VCE method. *Journal of Geophysical Research: Solid Earth*. <https://doi.org/10.1029/2018jb017159>
- Liu, P., Li, Z., Hoey, T., Kincal, C., Zhang, J., Zeng, Q., & Muller, J.-P. (2013). Using advanced InSAR time series techniques to monitor landslide movements in Badong of the Three Gorges region, China. *International Journal of Applied Earth Observation and Geoinformation*, 21, 253–264. <https://doi.org/10.1016/j.jag.2011.10.010>
- Michel, R., Avouac, J.-P., & Taboury, J. (1999). Measuring near field coseismic displacements from SAR images: Application to the Landers earthquake. *Geophysical Research Letters*, 26(19), 3017–3020. <https://doi.org/10.1029/1999gl900524>
- Murray, K. D., Lohman, R. B., Kim, J., & Holt, W. E. (2021). An alternative approach for constraining 3D-displacements with InSAR, applied to a fault-bounded groundwater entrainment field in California. *Journal of Geophysical Research: Solid Earth*, 126(5). <https://doi.org/10.1029/2020JB021137>
- NISAR. (2018). *NASA-ISRO SAR (NISAR) mission science Users' Handbook*. Jet Propulsion Laboratory, California Institute of Technology.
- Paronuzzi, P., Rigo, E., & Bolla, A. (2013). Influence of filling–drawdown cycles of the Vajont reservoir on Mt. Toc slope stability. *Geomorphology*, 191, 75–93. <https://doi.org/10.1016/j.geomorph.2013.03.004>
- Petley, D. (2012). Global patterns of loss of life from landslides. *Geology*, 40(10), 927–930. <https://doi.org/10.1130/g33217.1>
- Ren, K., Yao, X., Li, R., Zhou, Z., Yao, C., & Jiang, S. (2022). 3D displacement and deformation mechanism of deep-seated gravitational slope deformation revealed by InSAR: A case study in Wudongde reservoir, Jinsha river. *Landslides*, 19(9), 2159–2175. <https://doi.org/10.1007/s10346-022-01905-8>
- Rosen, P. A., Hensley, S., & Chen, C. (2010). Measurement and mitigation of the ionosphere in L-band interferometric SAR data. Paper presented at the 2010 IEEE radar conference.
- Samsonov, S. (2019). Three-dimensional deformation time series of glacier motion from multiple-aperture DInSAR observation. *Journal of Geodesy*, 93(12), 2651–2660. <https://doi.org/10.1007/s00190-019-01325-y>
- Shi, X., Hu, X., Sitar, N., Kayen, R., Qi, S., Jiang, H., et al. (2021). Hydrological control shift from river level to rainfall in the reactivated Guobu slope besides the Laxiwa hydropower station in China. *Remote Sensing of Environment*, 265, 112664. <https://doi.org/10.1016/j.rse.2021.112664>
- Shi, X., Jiang, H., Zhang, L., & Liao, M. (2017). Landslide displacement monitoring with split-bandwidth interferometry: A case study of the Shuping landslide in the three gorges area. *Remote Sensing*, 9(9), 937. <https://doi.org/10.3390/rs9090937>
- Shi, X., Liao, M., Li, M., Zhang, L., & Cunningham, C. (2016). Wide-area landslide deformation mapping with multi-path ALOS PALSAR data stacks: A case study of three gorges area, China. *Remote Sensing*, 8(2), 136. <https://doi.org/10.3390/rs8020136>
- Shi, X., Zhang, L., Balz, T., & Liao, M. (2015). Landslide deformation monitoring using point-like target offset tracking with multi-mode high-resolution TerraSAR-X data. *ISPRS Journal of Photogrammetry and Remote Sensing*, 105, 128–140. <https://doi.org/10.1016/j.isprsjprs.2015.03.017>
- Shi, X., Zhang, L., Tang, M., Li, M., & Liao, M. (2017). Investigating a reservoir bank slope displacement history with multi-frequency satellite SAR data. *Landslides*, 14(6), 1961–1973. <https://doi.org/10.1007/s10346-017-0846-3>
- Simons, M., Bekaert, D., Borsa, A., Donnellan, A., Fielding, E., Jones, C., & Zebker, H. (2021). *Nisar requirements and validation approach for solid Earth science*. Paper presented at the IEEE International Geoscience and Remote Sensing Symposium IGARSS, Brussels, Belgium.
- Tantianupurp, P., Shi, X., Zhang, L., Balz, T., & Liao, M. (2013). Characterization of landslide deformations in three gorges area using multiple InSAR data stacks. *Remote Sensing*, 5(6), 2704–2719. <https://doi.org/10.3390/rs5062704>
- Tomás, R., Li, Z., Liu, P., Singleton, A., Hoey, T., & Cheng, X. (2014). Spatiotemporal characteristics of the Huangtupo landslide in the Three Gorges region (China) constrained by radar interferometry. *Geophysical Journal International*, 197(1), 213–232. <https://doi.org/10.1093/gji/gju017>
- Wang, F.-W., Zhang, Y.-M., Huo, Z.-T., Matsumoto, T., & Huang, B.-L. (2004). The July 14, 2003 Qianjiangping landslide, three gorges reservoir, China. *Landslides*, 1(2). <https://doi.org/10.1007/s10346-004-0020-6>
- Wang, Y., Yang, Z., Li, Z., Zhu, J., & Wu, L. (2020). Fusing adjacent-track InSAR datasets to densify the temporal resolution of time-series 3-D displacement estimation over mining areas with a prior deformation model and a generalized weighting least-squares method. *Journal of Geodesy*, 94, 1–17. <https://doi.org/10.1007/s00190-020-01374-8>
- Wasowski, J., & Bovenga, F. (2015). Remote sensing of landslide motion with emphasis on satellite multitemporal interferometry applications (pp. 345–403). <https://doi.org/10.1016/b978-0-12-396452-6.00011-2>
- Wright, T. J. (2004). Toward mapping surface deformation in three dimensions using InSAR. *Geophysical Research Letters*, 31(1). <https://doi.org/10.1029/2003gl018827>
- Yang, Z., Li, Z., Zhu, J., Yi, H., Hu, J., & Feng, G. (2017). Deriving dynamic subsidence of coal mining areas using InSAR and logistic model. *Remote Sensing*, 9(2), 125. <https://doi.org/10.3390/rs9020125>
- Ye, X., Zhu, H.-H., Cheng, G., Pei, H.-F., Shi, B., Schenato, L., & Pasuto, A. (2023). Thermo-hydro-poro-mechanical responses of a reservoir-induced landslide tracked by high-resolution fiber optic sensing nerves. *Journal of Rock Mechanics and Geotechnical Engineering*. <https://doi.org/10.1016/j.jrmge.2023.04.004>
- Zhang, L., Liao, M., Balz, T., Shi, X., & Jiang, Y. (2015). Monitoring landslide activities in the three gorges area with multi-frequency satellite SAR data sets. *Modern Technologies for Landslide Monitoring and Prediction*, 181–208. [https://doi.org/10.1007/978-3-662-45931-7\\_10](https://doi.org/10.1007/978-3-662-45931-7_10)
- Zhang, Q., Huang, G., Du, Y., & Bai, Z. (2022a). Raw GNSS observations of the 2019–2021 Xinpu landslide, Three Gorges Reservoir area, China (in Chinese). <https://doi.org/10.11878/db.202206.006947>
- Zhang, Q., Huang, G., Du, Y., & Bai, Z. (2022b). Three-dimensional deformation of the Xinpu landslide in the Three Gorges Reservoir Area, China, based on GNSS measurements from 2019–2021 (in Chinese). <https://doi.org/10.11878/db.202206.006948>
- Zheng, W., Hu, J., Liu, J., Sun, Q., Li, Z., Zhu, J., & Wu, L. (2021). Mapping complete three-dimensional ice velocities by integrating multi-baseline and multi-aperture InSAR measurements: A case study of the grove mountains area, east Antarctic. *Remote Sensing*, 13(4), 643. <https://doi.org/10.3390/rs13040643>
- Zheng, W., Hu, J., Zhang, W., Yang, C., Li, Z., & Zhu, J. (2017). Potential of geosynchronous SAR interferometric measurements in estimating three-dimensional surface displacements. *Science China Information Sciences*, 60(6). <https://doi.org/10.1007/s11432-016-9079-8>